DAVID W. TAYLOR NAVAL SHIP RESEARCH AND DEVELOPMENT CENTER

Bethesda, Maryland 20084

TIP VORTEX CAVITATION CHARACTERISTICS AND DELAY OF INCEPTION ON A THREE—DIMENSIONAL HYDROFOIL

by

William G. Souders
Gregory P. Platzer

APPROVED FOR PUBLIC RELEASE: DISTRIBUTION UNLIMITED

SHIP PERFORMANCE DEPARTMENT
RESEARCH AND DEVELOPMENT REPORT

WHOI
DOCUMENT
COLLECTION

April 1981   DTNSRDC-81/007

MAJOR DTNSRDC ORGANIZATIONAL COMPONENTS
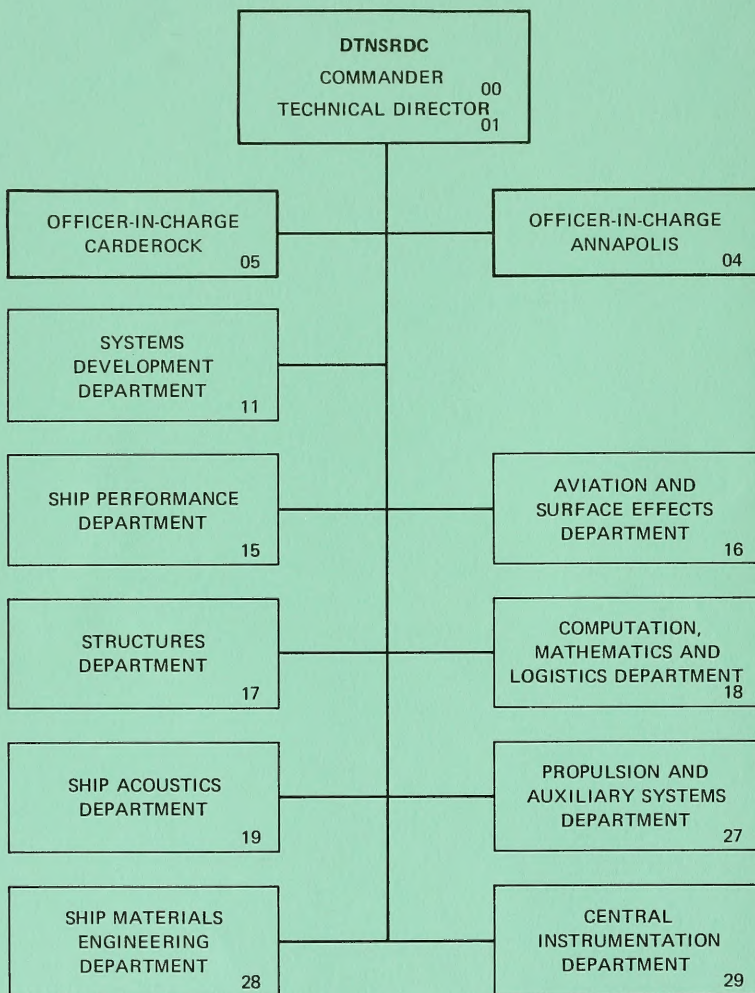
DTNSRDC

COMMANDER 00

TECHNICAL DIRECTOR 01

OFFICER-IN-CHARGE
CARDEROCK 05

OFFICER-IN-CHARGE
ANNAPOLIS 04

SYSTEMS
DEVELOPMENT
DEPARTMENT 11

SHIP PERFORMANCE
DEPARTMENT 15

AVIATION AND
SURFACE EFFECTS
DEPARTMENT 16

STRUCTURES
DEPARTMENT 17

COMPUTATION,
MATHEMATICS AND
LOGISTICS DEPARTMENT 18

SHIP ACOUSTICS
DEPARTMENT 19

PROPULSION AND
AUXILIARY SYSTEMS
DEPARTMENT 27

SHIP MATERIALS
ENGINEERING
DEPARTMENT 28

CENTRAL
INSTRUMENTATION
DEPARTMENT 29

Dept. of
O. E.   APR 30 1981

REPORT DOCUMENTATION PAGE		READ INSTRUCTIONS BEFORE COMPLETING FORM
1. REPORT NUMBER DTNSRDC-81/007	2. GOVT ACCESSION NO.	3. RECIPIENT'S CATALOG NUMBER
4. TITLE (and Subtitle) TIP VORTEX CAVITATION CHARACTERISTICS AND DELAY OF INCEPTION ON A THREE-DIMENSIONAL HYDROFOIL		5. TYPE OF REPORT & PERIOD COVERED Research and Development
		6. PERFORMING ORG. REPORT NUMBER
7. AUTHOR(s) William G. Souders Gregory P. Platzer		8. CONTRACT OR GRANT NUMBER(s)
9. PERFORMING ORGANIZATION NAME AND ADDRESS David W. Taylor Naval Ship Research and Development Center Bethesda, Maryland 20084		10. PROGRAM ELEMENT, PROJECT, TASK AREA & WORK UNIT NUMBERS (See reverse side)
11. CONTROLLING OFFICE NAME AND ADDRESS David W. Taylor Naval Ship Research and Development Center Bethesda, Maryland 20084		12. REPORT DATE April 1981
		13. NUMBER OF PAGES 65
14. MONITORING AGENCY NAME & ADDRESS(if different from Controlling Office) Naval Material Command Washington, DC 20360		15. SECURITY CLASS. (of this report) UNCLASSIFIED
		15a. DECLASSIFICATION/DOWNGRADING SCHEDULE

16. DISTRIBUTION STATEMENT (of this Report)

APPROVED FOR PUBLIC RELEASE: DISTRIBUTION UNLIMITED

17. DISTRIBUTION STATEMENT (of the abstract entered in Block 20, if different from Report)

18. SUPPLEMENTARY NOTES

19. KEY WORDS (Continue on reverse side if necessary and identify by block number)

Tip Vortex Cavitation
Tip Vortex Cavitation Delay
Marine Lifting Surfaces
Performance

Mass Injected Tip
Roughened Tip
Bulbous Tip

20. ABSTRACT (Continue on reverse side if necessary and identify by block number)

A research program was conducted to investigate both the fundame tal aspects of, and techniques for delaying, tip vortex cavitation on a three-dimensional hydrofoil. The specific concepts considered for delaying tip vortex cavitation included: a bulbous tip, an artifically roughened tip, and a mass injected tip. The experiments were conducted in the David W. Taylor

(Continued on reverse side)

DD FORM 1473   EDITION OF 1 NOV 65 IS OBSOLETE
1 JAN 73   S/N 0102-LF-014-6601

(Block 10)

    Program Element 62543N
    Task Area ZF 43-421-001
    Work Unit 1500-104

(Block 20 continued)

Naval Ship Research and Development Center 24-inch cavitation tunnel, where
the effects of the various concepts on both foil tip vortex cavitation in-
ception and performance were established. These measurements were made at a

Reynolds number R_c, based on root chord length, of approximately 5×10^6.

    Some of the more fundamental aspects of the tip vortex rollup process
have been documented through the use of flow visualization techniques. The
results for the tip vortex cavitation delay concepts indicate substantial
increases in the tip vortex cavitation inception speed relative to the un-
altered tip; i.e., a 94 percent increase for the roughened tip, 38 percent
for the bulbous tip, and 54 percent and 33 percent for the active and
passive mass injected tips respectively. These results were obtained over
a wide range of foil angle of attack and with little or no measurable loss
in foil performance; i.e., no measurable lift decrease or drag increase.

TABLE OF CONTENTS

LIST OF FIGURES

LIST OF ABBREVIATIONS AND SYMBOLS

a_c Tip vortex core radius

A   Planform area

AMI   Active mass injection

AR   Aspect ratio

c   Local section chord length

C   Root chord length

C_D Drag coefficient, $\dfrac{D}{\frac{1}{2}\rho U^2 A}$

C_L Lift coefficient, $\dfrac{L}{\frac{1}{2}\rho U^2 A}$

D   Drag, parallel to U

f   Section camber

k   Constant in Equation (1)

ℓ Local spanwise load

L   Lift, normal to U

m   Lift curve slope

P_v Vapor pressure

P_∞ Free stream static pressure

PMI   Passive mass injection

Q   Mass flow rate

R_c Reynolds number based on C, $U\dfrac{C}{\nu}$

S   Semispan

t   Maximum section thickness

TVC   Tip vortex cavitation

U	Free stream velocity
U_P	TVC inception speed of parent foil
U_β	TVC inception speed of the particular concept
U_i	Mass injection velocity
V_T	Tip vortex tangential velocity
VPWT	Variable pressure water tunnel
x	Chordwise distance from leading edge
x_t	Transistion distance from leading edge
Y	Spanwise distance from foil root
Yrm	Roll moment arm
α	Angle of attack
ρ	Fluid density
σ	Cavitation index, $\dfrac{(P_\infty - P_v)}{\frac{1}{2}\rho U^2}$
ν	Fluid kinematic viscosity

ABSTRACT

A research program was conducted to investigate both the fundamental aspects of, and techniques for delaying, tip vortex cavitation on a three-dimensional hydrofoil. The specific concepts considered for delaying tip vortex cavitation included: a bulbous tip, an artificially roughened tip, and a mass injected tip. The experiments were conducted in the David W. Taylor Naval Ship Research and Development Center 24-inch cavitation tunnel, where the effects of the various concepts on both foil tip vortex cavitation inception and performance were established. These measurements were made at a Reynolds number R_c, based on root chord length, of approximately 5×10^6.

Some of the more fundamental aspects of the tip vortex rollup proccess have been documented through the use of flow visualization techniques. The results for the tip vortex cavitation delay concepts indicate substantial increases in the tip vortex cavitation inception speed relative to the unaltered tip; i.e., a 94 percent increase for the roughened tip, 38 percent for the bulbous tip, and 54 percent and 33 percent for the active and passive mass injected tips respectively. These results were obtained over a wide range of foil angle of attack and with little or no measurable loss in foil performance; i.e., no measurable lift decrease or drag increase.

ADMINISTRATIVE INFORMATION

INTRODUCTION

On a lifting surface of finite span, pressure gradients of opposite signs exist on the pressure and suction sides. The span-wise velocity components at the tip are similarly of opposite sign, creating a vortex located at the foil tip, as shown in Figure 1. This tip vortex phenomenon presents special problems in practically all applications of winglike bodies; e.g., the noise and vibration caused by the interaction of the concentrated tip vortex trailed from the tip of a helicopter rotor with a following blade and the potential hazard associated with the loss of control of light aircraft which follow in the trailing tip vortex wake of heavier aircraft. Additionally, in the case of marine lifting surfaces, this phenomemon

1
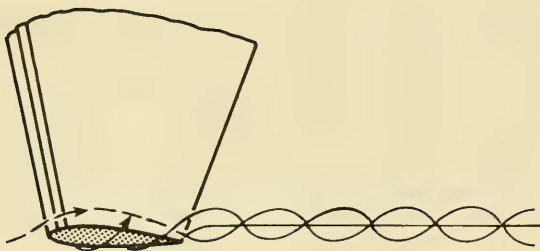
Figure 1 — Tip-Vortex Rollup Process

can lead to the situation where the local pressure in the tip vortex core reduces
to the vapor pressure of the liquid, resulting in cavitation and its attendant
problems.

Several years ago, a research program was initiated to develop techniques for
designing marine lifting surfaces with delayed/improved tip vortex cavitation
(TVC) performance. The first phase of this program was devoted to a study of the
pertinent literature and the establishment of a technology base. In this survey,[1*]
over 150 tip-vortex-related documents were identified and cataloged. In addition,
those concepts which held promise for the delay of TVC on marine lifting surfaces
were given close attention and appropriate experimental investigations were recom-
mended. The second phase of the program involved carrying out the recommended ex-
perimental investigation.

This report presents the results of the TVC experimental program. The specific
concepts recommended for evaluation included: a bulbous tip having a selective in-
crease in the foil tip thickness, an artifically roughened tip, and a mass injected
tip with the introduction of fluid directly into the tip vortex core. A detailed
description of these devices is presented in the following sections. The experiment
was conducted in the DTNSRDC 24-inch cavitation tunnel using a three-dimensional
hydrofoil model. Initially, efforts were directed toward gaining some fundamental
insight into both the tip vortex rollup and cavitation process. The results from
this initial work guided the design of the specific concepts discussed above and in-
cluded flow visualization techniques; e.g., tufts, photography and paint flow.

*A complete listing of references is given on page 53.

2

Each concept has been evaluated in the cavitation tunnel and includes measurements of both tip vortex cavitation inception and performance—lift, drag, and roll moment. These measurements were made at a Reyonlds number R_c of approximately 5×10^6.

REPRESENTATION OF THE TIP-VORTEX ROLLUP PROCESS

The importance of tip vortices in fluid mechanics is demonstrated by the wealth of literature[1] dealing with the subject. In the past, an accurate mathematical representation of the tip-vortex rollup phenomenon has been limited by the difficulties in handling the complicated three-dimensional aspects of the tip crossflows and the turbulent vortex. Today, as more detailed experimental data become available and numerical techniques become more sophisticated, the ability of the analytical models to predict the observed tip vortices is being improved.

The first generation of models[2] to represent the vortex rollup phenomenon consisted of a simplified semi-two-dimensional theory, where a vortex sheet emanates from the trailing edge of a wing and rolls up into a concentrated vortex under the action of its self-induced velocity field. The strength of the vortex is determined by the spanwise load distribution of the wing. This simplified model failed to correctly predict the size and stength of observed vortices.

As more experimental data emerged, the later models became more realistic and elaborate; for example velocity surveys[3] of tip vortices indicated a tangential velocity distribution (as shown in Figure 2). These data identified an inner core with a rotational vortex structure which is surrounded by an irrotational vortex region. Incorporation of this observed vortex structure gave rise to a second generation vortex model. However, this model also failed to predict the observed vortices, due in part to an inability to predict the core radius. Continued experimental work[4] led to the hypothesis that the tip vortex core radius was a function of the boundary layer on the wing tip surface. Later work[5] substantiated this hypothesis. The effects of the tip boundary layer characteristics on both the tip vortex tangential velocity and core radius are illustrated in Figure 3. Here, a comparsion is made between a laminar boundary layer tip flow—untripped—and a turbulent boundary layer tip flow—tripped. The data[5] indicate that the thicker turbulent boundary layer on the pressure side of the wing tip results in an increased tip vortex core radius and a decrease in the tip vortex maximum tangential velocity as compared to

3
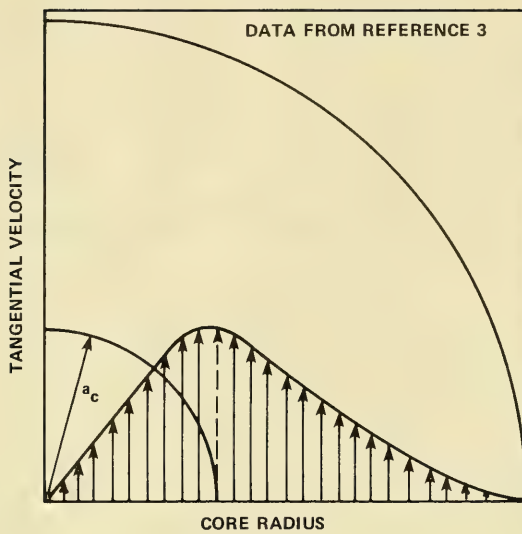
Figure 2 – Tip Vortex Tangential Velocity Distribution
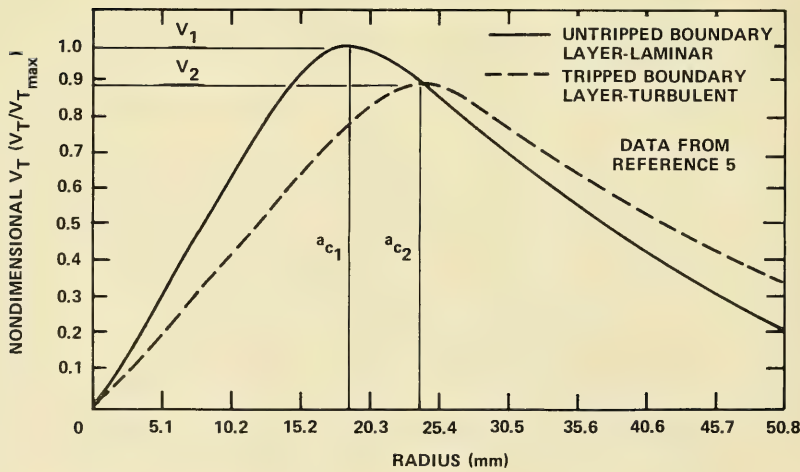
Figure 3 – Tip Vortex Tangential Velocity as a Function of Core Radius
for Laminar and Turbulent Flow

4

the laminar flow case. Note that $V_T/V_{T_{max}}$ is less than 1.0 for the turbulent flow because $V_{T_{max}}$ is based on the laminar flow case.

Further experimental research[6] revealed an axial velocity in the vortex core, which basically introduced a three dimensionality to the models. A third generation model[7] incorporating this observed phenomenon also failed to correctly predict the observed vortices. This disagreement was not totally unexpected because the theory is confined to laminar flow, which renders comparison with high Reynolds number, turbulent flow experiments somewhat uncertain.

The models representing the vortex sheet rollup are becoming more elaborate. However, they cannot, in general, predict vortices which are observed forward of the trailing edge. Pressures measured on the surface of a wing tip[8] indicated the presence of a concentrated vortex located just above the wing tip. A detailed mapping of the flowfield about a wing tip was made[9] using a small, hot, wire probe and, as shown in Figure 4, the results indicate that the vorticity generated in the pressure-side boundary layer migrates around the tip to the suction side of the wing tip. This vorticity in combination with the surrounding flow induces an outward flow on the surface of the wing tip suction side. This experimental visualization of the vortex rollup process indicates the importance of the detailed tip flow on the resulting vortex structure. A recent numerical approach[10] incorporating such parameters as local tip geometry, viscosity, and turbulence effects has duplicated these observed tip flow patterns. With the tools now available, it would appear that a more realistic fourth generation tip vortex model is not far away.

However, at this time, an analytical description of both the tip vortex rollup process and the prediction of TVC inception are not yet available. As a result, the major efforts in this area by McCormick[4] and Chandrashekhara,[11] as summarized by Noordzij,[12] involve formulations which are semiempirical in nature and require supporting experimental data. These formulations do, however, emphasize the dependence of the tip vortex rollup process upon the detailed flow at the wing tip and the overall spanwise load distribution. Also of importance is the strong influence of varying environmental conditions (i.e., changes in the size of the undisolved air nuclei) upon the TVC inception data. However, assuming that the influence of such environmental factors is small and that the vorticity entrained into the tip vortex
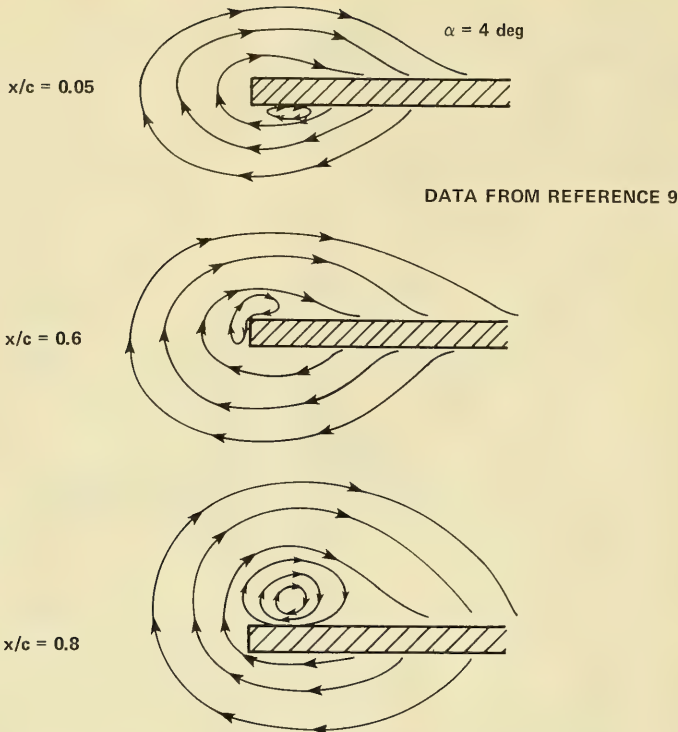
Figure 4 – Mapping of the Flowfield About a Wing Tip for
Various Nondimensional Chordwise Distances

dominates the shape of the σ versus C_L curve, the expected[11] variation of σ with C_L should be of the form

$$\sigma = kC_L^2 \tag{1}$$

The constant k is governed by the local geometric and boundary layer characteristic at the foil tip. This relationship has been used successfully in the current study and also proved convenient for comparing the TVC inception merits of the various concepts.

6

CONCEPTS FOR DELAYING TIP VORTEX CAVITATION

The results of the literature survey[1] identified approximately 20 concepts for alleviating tip vortices. Since a majority of the concepts were directly related to work in the aircraft industry, few were suited for marine applications where such factors as structural suitability, reliability, and operational environment had to be considered. Additionally, the problem for the two industries are somewhat different in that the aircraft industry seeks to dissipate the energy of the entire tip vortex wake, while the marine industry generally seeks only to increase the tip vortex core pressure to alleviate cavitation. However, the major limiting factor when considering marine application is that the device should not be a source of any additional local cavitation and should not introduce prohibitive performance penalties. Those concepts which appeared to meet the above considerations were recommended for experimental evaluation and are included in the current research. A general discussion of these devices follows--a more physical description will be given later.

THE BULBOUS AND ROUGHENED TIPS

These two concepts exploit the hypothesis[4] that the thickness of the foil tip viscous boundary layer plays an important role in the occurrence of tip vortex cavitation. For the bulbous tip, (defined as any selective increase in the foil tip thickness), the increased surface area results in a thicker tip viscous boundary layer which increases the viscous mass flow entering the vortex core. This, in turn, accelerates the dissipation of the vortex core energy. In addition, the bulb acts in a manner similar to an endplate and retards the tip vortex rollup process. The bulbous tip concept has been previously applied[13] to both model and full-scale marine lifting surfaces and although the results are promising, the bulb must be carefully designed to minimize both local surface cavitation and efficiency loss.

Similarly, the artifically roughened tip increases the thickness of the viscous boundary layer flow entering the tip vortex core, thus destabilizing the vortex core energy. Although relatively little attention has been given to this idea, an earlier qualitative study[4] did report that a roughened surface on the pressure side of the foil can substantially reduce the tip vortex cavitation inception index. Although no supporting performance data were reported, the concept warranted further pursuit.

THE MASS INJECTED TIP--ACTIVE AND PASSIVE

As implied, tip mass injection involves the ejection of a fluid, linearly down-stream, directly into the tip vortex core. The mass injection process increases the vortex core axial pressure and accelerates the vortex decay through the viscous interaction of the irrotational jet and the rotational vortex core. The effective-ness of this device has been demonstrated[14] repeatedly in air flow studies with little or no effect on wing or rotor performance. Although there is no data on the correlation between the water mass injection rates required to delay tip vortex cavitation and the reported air mass rates required to reduce vortex core vorticity, this active concept may prove to be an effective means of delaying tip vortex cavita-tion if the required delivery rates or power are small.

The above mass injection scheme will obviously require an energy source. A somewhat similar concept--the passive mass injected tip--requires no external energy source and consists of a hole or channel connecting the foil tip pressure and suction sides. The objective is to locate the hole in such a fashion that mass flow is diverted from the tip pressure side directly into the forming tip vortex core on the foil suction side. This concept, which evloved out of the literature survey,[1] is new. However, the idea was obtained from work[15] in the aircraft industry for porous wing tips. The success of the passive mass injection tip will depend upon the crit-ical location and orientation of the channel and the magnitude of the diverted mass flow.

METHODS AND PROCEDURES

FACILITY

The tip vortex delay study was conducted in the DTNSRDC 24-inch variable pres-sure water tunnel (VPWT). This tunnel is a closed-duct circuit oriented in a vert-ical plane in which water is circulated by a motor-driven impeller located in the lower horizontal leg. The tunnel capacity is 13,600 gal (51.5 m^3) and the maximum water speed is 44 ft/sec (13.4 m/sec). Tunnel pressure--0 to 35 psia (0 to 2.38 × 10^5 Pa)--was varied by changing the air pressure on the water surface at the top of the tunnel. The water level is automatically maintained at a constant 3.42 ft (1.04 m) above the centerline of the test section.

A 27-in. (0.686-m) diameter, semiclosed jet test section was used for the tip vortex experiments in the 24-in. VPWT. This test section had a conic transition to horizontal walls which produced approximately uniform flow over the hydrofoil.

Plexiglass windows at the sides of the test section permitted visual observation and photographic coverage of the hydrofoil models. During model testing, the test section velocity was measured by a single pitot-static tube mounted in 2-D test section just upstream and below the model. Figure 5 shows a schematic of the model and the semiclosed jet test section in the 24-in. VPWT.
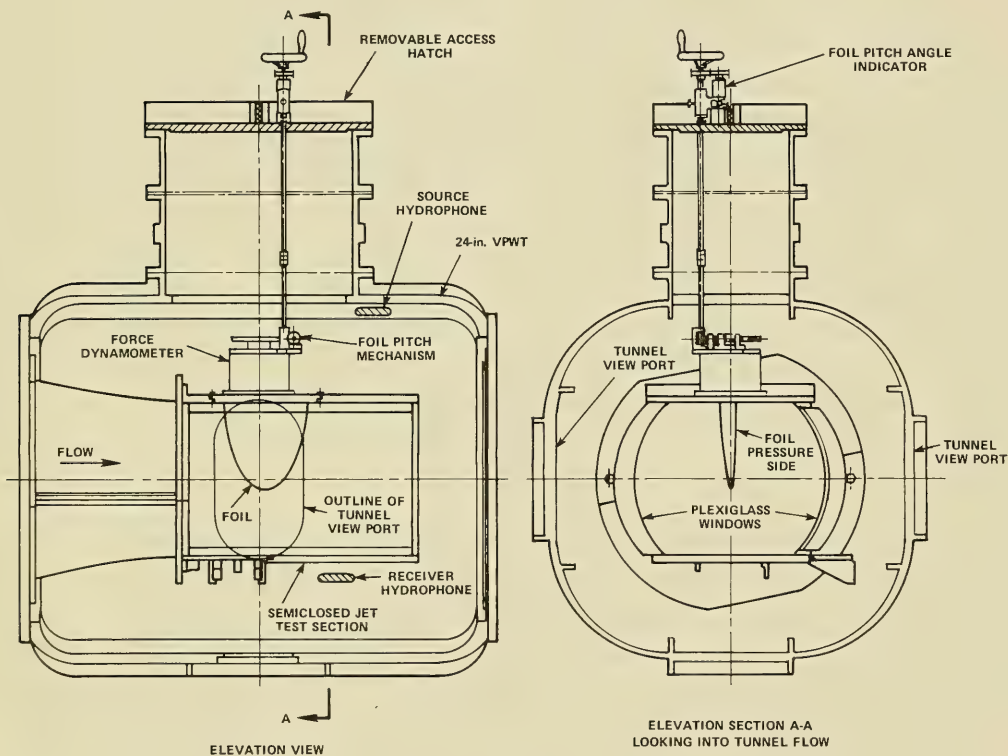

Figure 5 – Schematic of 24-Inch Variable Pressure Water Tunnel
Arrangement Showing Semiclosed Jet Test
Section and Model

MODELS

The following is a physical description of the tip vortex cavitation delay models. The criteria used in determining these specific designs will be discussed later.

The hydrofoil models used for the present study are all identical except the various local tip modifications:

Parent

The parent hydrofoil had an elliptical planform with a semispan and root chord length of 12 in. (0.305 m), giving an aspect ratio AR = 2.55 for full-span flow, as approximated by the test section wall. The cambered airfoil section of the hydro-foil consisted of NACA-66 (DTNSRDC modified) thickness distribution with a NACA a = 0.8 meanline camber distribution. The hydrofoil had a constant spanwise thickness to chord ratio $t/c = 0.10$ and a constant spanwise camber to chord ratio $f/c = 0.025$. A sketch of the airfoil section and a listing of nondimensional section offsets is given in Figure 6. In addition, the hydrofoil had a design lift coefficient (all lift due to camber) $C_L = 0.186$ at an angle of attack $\alpha = 0.567$ deg. The models were cast with an aluminum alloy and precision machined using numerical control techniques. Grids, consisting of a series of chordwise and spanwise lines of known thickness and spacing, were penciled on the anodized foil surfaces.

Bulb

The two bulb modifications were limited to the tip region of the hydrofoil; i.e., spanwise 2.4 in. (0.061 m) and 2.0 in. (0.051 m) inboard from the tip for the large and small bulb, respectively. The bulbs consisted of thickened airfoil sections similar to the parent with chord lengths equal to the parent foil. The maximum thickness of the bulbs was 1.6 in. (0.041 m) and 0.8 in. (0.020 m), respectively, at a spanwise distance inboard from the tip of 0.8 in. (0.020 m) where the corresponding parent thickness was 0.43 in. (0.011 m). Figure 7 shows a photograph and a plot of the thickness distribution of the two bulbs.

Roughness

The roughness was applied to the extreme tip area of the parent foil pressure and suction sides. For the optimum distribution, the pressure side application was
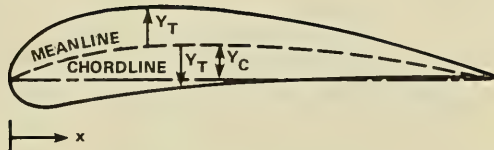
$$Y_T = Y_T/\tau \cdot t/c \cdot c = Y_T/\tau \cdot (0.10) \cdot c$$

$$Y_c = Y_c/f \cdot fm/c \cdot c = Y_c/\tau \cdot (0.025) \cdot c$$

WHERE

fm = CAMBER
t = THICKNESS
C = CHORD

AND LEADING EDGE RADIUS = $0.448 \, (t/c)^2 \cdot C$

X/C	Y_T/τ	Y_c/f
0	0	0
0.025	0.1466	0.1586
0.050	0.2066	0.2712
0.100	0.2907	0.4482
0.200	0.4000	0.6993
0.300	0.4637	0.8635
0.400	0.4962	0.9615
0.500	0.4962	1.0000
0.600	0.4653	0.9786
0.700	0.4035	0.8892
0.800	0.3110	0.7027
0.900	0.1877	0.3586
1.000	0.0333	0.0000

Figure 6 – Nondimensional Section Offets of the Parent Foil
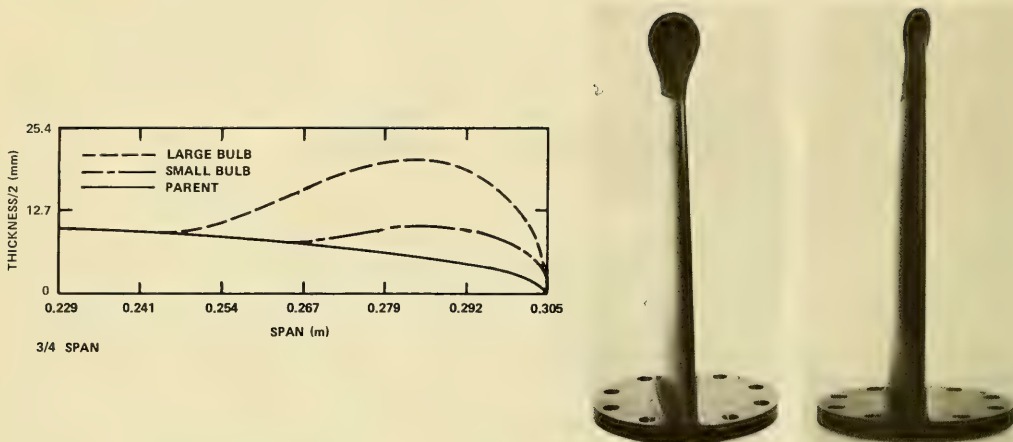
Figure 7 – Photograph and Spanwise Thickness Distribution for
the Small and Large Bulbous Tips

limited to the area 0.5 in. (0.013 m) inboard from the tip, corresponding to an
area of approximately 0.7 percent of the total pressure side area; for the suction
side, application was limited to the area 0.25 in. (0.006 m) inboard from the tip,
representing an area of approximately one-half of that treated on the pressure side.
These optimum areas of application were determined from paint flow studies and will
be discussed later.   The following roughness configurations were evaluated: pressure
side only, suction side only and both pressure and suction sides.   A range of rough-
ness heights was obtained by using percision grain size silicon carbide, 90–800
microns, which was applied with two-stage epoxy resin and easily removed with appro-
priate epoxy stripper.   Figure 8 is a photograph showing an overall and closeup view
of 600 micron roughness applied to the parent foil pressure side.

Mass Injection

        For the passive mass injection foil, a channel was fabricated through the tip
connecting the foil pressure and suction sides and aligned with the free stream flow.

12.7 mm

12.7 mm
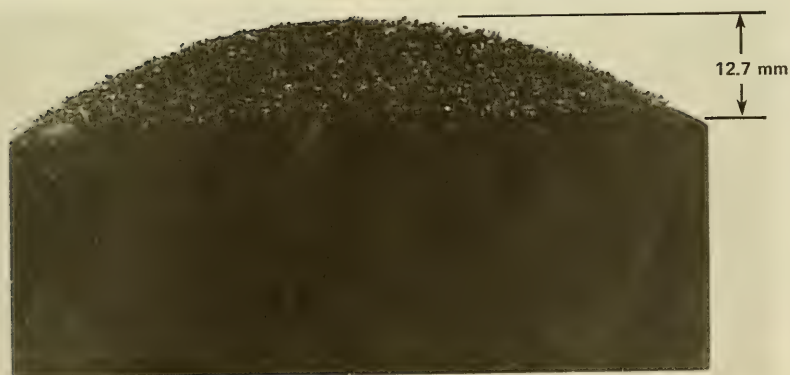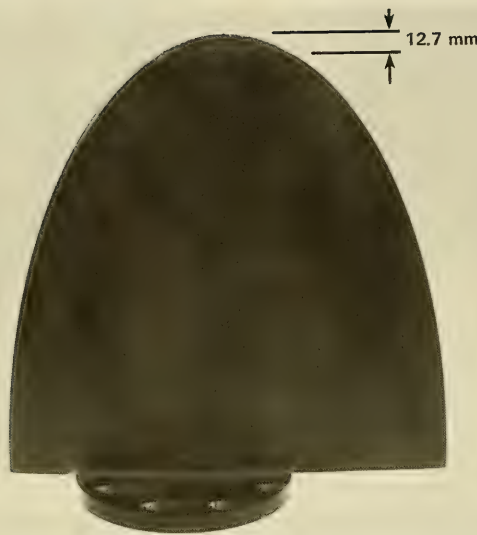
Figure 8 – Overall and Closeup Views of 600 Micron Roughness Applied
to the Parent Foil Pressure Side

13

The hole exited on the suction side at the location of the observed tip vortex attachment point--at the foil midchord and approximately 0.10 in. (0.00254 m) inboard of the tip. Two channel diameters were investigated, 0.125 in. (0.0032 m) and 0.188 in. (0.0048 m), and they were drilled at an angle of 10 deg with respect to the foil chordline. Figure 9 shows an overall view and a tip closeup of the 0.125 in. (0.0032 m) channel model.

For the active mass injection foil, a tube or nozzle was fabricated into the foil suction side tip--in close vicinity of the tip vortex attachment point--which enabled water to be injected, downstream, directly into the tip vortex core. The end of the injection nozzle was located at midchord, inboard approximately 0.072 in. (0.00183 m) from the tip, and oriented in a chordwise direction. This tube, with a 0.133 in. (0.00338 m) outside diameter, was fitted and faired into a channel which was cut into the surface of the foil tip. Inside the foil, the tube connected to a larger feed-line which extended the entire span of the model. Figure 10 shows a closeup of the active mass injection tip area.

The active mass injection pumping system consisted of a turbine pump--Aurora, 20 gal/min (0.0751 m^3/min) at 350 ft (160.7 m) head--a flow meter, relief and control valves, etc. Water was taken from the lower branch of the 24-in. VPWT and pumped to the foil injection nozzel at flow rates ranging from 0.3 to 2.4 gal/min (1.13×10^{-3} to 9.07×10^{-3} m^3/min).

MEASURING AND MOUNTING APPARATUS

The model mounting and measuring apparatus is shown schematically in Figure 5. Photographs of the assembled components are shown in Figure 11. The apparatus bolted to a rectangular mounting plate which fitted flush into the top of the 2-D test section wall. The models bolted directly to a strain gaged force dynamometer, enclosed in the cylindrical housing, which sensed forces normal and tangential to the foil chord. Also, the roll moment associated with the normal force was measured. The dynamometer, designed to accommodate a maximum normal and tangential force of 1000 and 80 lb (4450 to 356 N), respectively, was supported by bearings which allowed rotation about an axis through 40 percent root foil chord--through a series of reduction gears. As shown, the model angle of attack could be changed from outside the tunnel through the use of a handcrank and an extension rod. Model access was obtained by lifting the apparatus, as shown in Figure 5, out through the tunnel access hatch.

14
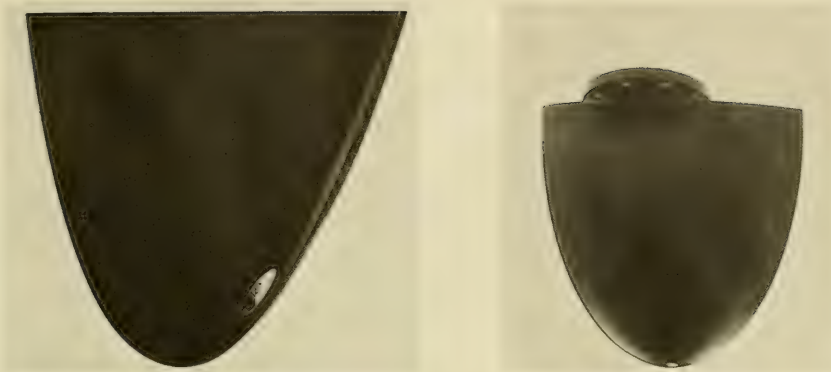
Figure 9 — Passive Mass Injection Tip
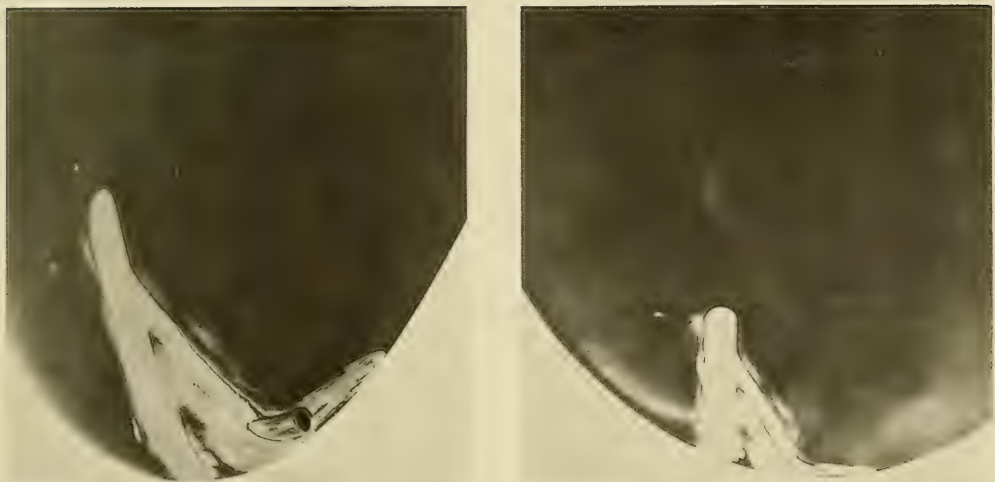

Figure 10 — Active Mass Injection Nozzle
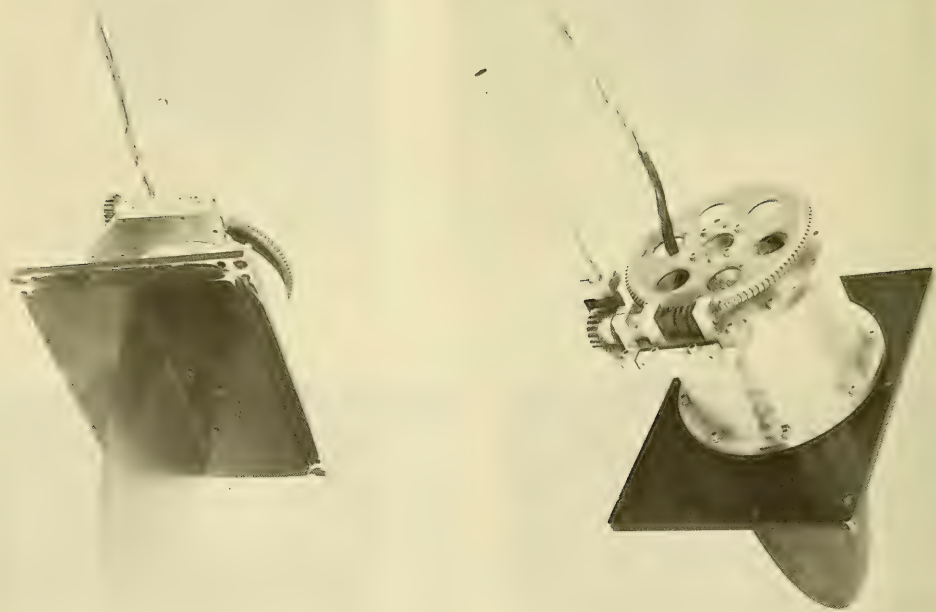
Figure 11 - Model Mounting and Measuring Apparatus

The following is a brief description of the equipment utilized in the present study. For the 2-D test section velocity survey, to be discussed later, the pressures from both the rake pitot tubes and the tunnel venturi taps were sensed by Validyne variable reluctance pressure transducers. Both the pressure gauge and strain gauge force dynamometer analog signals were conditioned with Endevco carrier demodulators and Dana-Ectron dc amplifiers. These conditioned signals then were processed by a Vidar integrating digital voltmeter and printer.

The test section velocity was also determined by the use of a single pitot-static tube and a mercury manometer. Mercury manometers were used to measure the tunnel static pressure--the pressure of the air above the water in the tunnel. The tunnel water temperature, the tunnel air content, and the atmospheric pressure were determined from meters permanently installed at the tunnel.

FLOW VISUALIZATION

As discussed earlier, the use of the various concepts to delay tip vortex cavitation is predicated upon some basic knowledge of the viscous rollup process. Accordingly, the initial experimental efforts were devoted to flow visualization studies. Three flow visualization techniques were employed. First, tufts were used to define the gross flow (i.e., outside the foil boundary layer) over the model. The tufts, consisting of a rather dense matrix of approximately 1/2-in. (0.0127-m) long segments of yarn, were cemented to the foil surface. When subjected to flow, the tuft orientation was sketched in relation to the grid marked on the foil surface. Second, paint flow studies were conducted to determine the flow characteristics in the model boundary layer--on the foil surface. This technique involved the application of a viscous mixture, equal parts by weight, of 90 SAE motor oil and fluorescent pigments to the leading edge of the model. When subjected to flow, this mixture migrated over the foil surfaces, leaving a detailed and permanent pattern of the flow. These patterns were studied and documented with photographs. Third, photography (both stills and movies) was used to capture the various stages of tip vortex cavitation development, particularly the tip vortex attachment point on the   . Selective results of the flow visualization work will be presented late

EXPERIMENTAL PROCEDURES

Before the tip vortex studies commenced, the nature of the flow across the 2-D test section was established. The velocity profile across the test section was determined from pitot tube rake measurements. These measurements were correlated with both tunnel impeller rpm and venturi pressure drop--taken in the converging section of the tunnel just upstream of the test section. The pitot tube rake contained five Prandtl-type pitot tubes and extended over one-half of the 2-D test section height; vertical flow symmetry was assumed. The velocity calibration, made at atmospheric pressure, showed that the highest velocity occurred nearest the wall, with monotonically decreasing values toward the center. Since the highest and lowest velocities differed by no more than 2.0 percent on the average, the linear average of the five readings was taken as representative of section flow speed. Maximum speed obtained during calibration was 44 ft/sec (13.41 m/sec) which corresponded to a tunnel impeller rpm of 325. Several representative velocity profiles across the 2-D test section are shown in Figure 12. Since blockage effects were estimated[16] to be small, (approximately 1 percent) and since interest was focused on relative results, blockage corrections were not considered necessary.

For the flow visualization experiments, a thin strip of the oil-fluorescent pigment material was applied to the leading edge, both pressure and suction side, of the parent hydrofoil. The model was installed in the tunnel and the flow was quickly accelerated to a maximum velocity of 44 ft/sec (13.41 m/sec). An exposure time of only a few seconds at this velocity was necessary for the mixture to migrate to a steady state condition over the foil surfaces, after which the flow was quickly decelerated to zero. This procedure was followed for model angles of attack of 0.5 (design), 10 and, -3 degrees. Supporting efforts also included the use of tufts and photography, both stills and motion picture.

The performance of each hydrofoil was established by measuring the lift, drag, and roll moment. These load measurements were made at two speeds, U = 25 and 44 ft/sec (7.62 and 13.41 m/sec) and at angles of attack 10 deg $\geq$ a $\geq$ -7 deg in 1-deg increments. For these measurements the tunnel static absolute pressure was kept high, about 50 in. (1.27 m) of mercury, in order to avoid model surface cavitation. The force data was found to be repeatable within 2 percent for lift and 3 percent for drag.

The cavitation inception measurements for each model hydrofoil were taken at the maximum tunnel speed U = 44 ft/sec (13.41 m/sec) and at an air content level of
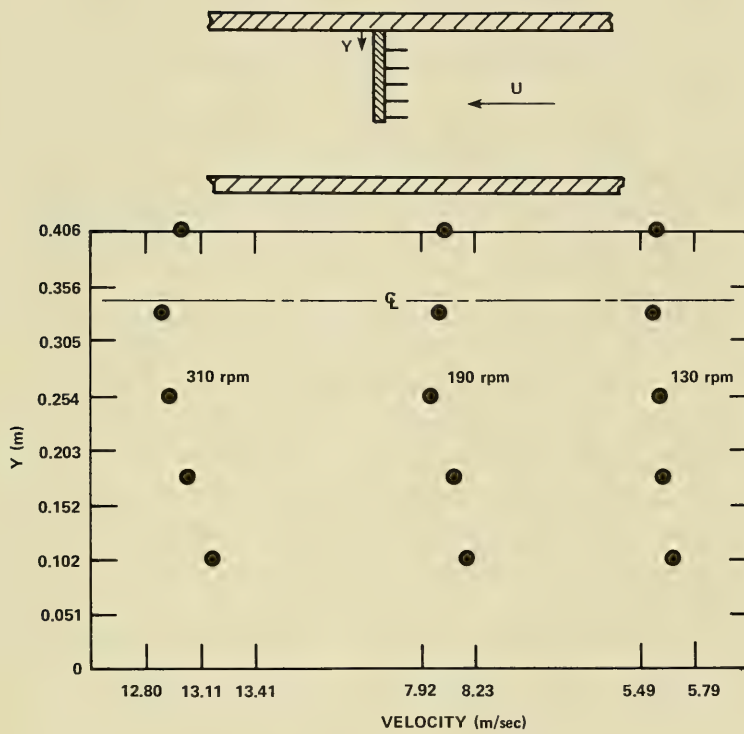
Figure 12 – Velocity Profiles Across Two-Dimensional Test Section

about 40 percent of saturation at atmospheric pressure. This air content level was the minimum obtainable and generally limited the tunnel working pressure, for visually calling cavitation inception, to a minimum absolute pressure of 12 in. (0.305 m) of mercury. This tunnel pressure limitation also limited the investigative range of angle of attack to $-6.\deg \leq \alpha \leq 4$ deg. Procedurally, for a set α and U, the tunnel pressure was lowered to the point where tip vortex cavitation was observed--usually in the vortex wake. Then, the tunnel pressure was increased arbitrarily until the cavitation disappeared and this pressure was recorded. This procedure was repeated twice and the average of the three pressures was taken to be the inception pressure for this condition. The tip vortex cavitation was well-defined visually with the aid of appropriate back lighting. The model angle of attack then was changed in 1/2-deg increments, and the inception procedure was repeated. Due to the unsteady nature of the cavitation at inception, desinence and inception are equivalent.

RESULTS AND DISCUSSION

The results of the tip vortex study are presented in two sections. The first section presents the results of the basic aspects of the tip vortex study. This work was performed on the parent or unaltered hydrofoil and included flow visualization, forces and TVC inception. The second section, which was based upon the results of the first, presents the results of the various TVC delay concepts and includes primarily force and TVC inception data. Also included in this section is a brief dicussion of the rationale which lead to the specific design of the particular concept.

TIP VORTEX CHARACTERISTICS--PARENT FOIL FLOW VISUALIZATION

As discussed earlier, the use of the various concepts to delay tip vortex cavitation is predicated upon some basic knowledge of the viscous rollup process. For example, both the active and passive mass injection schemes require precise positioning of the nozzle to insure injection directly into the vortex core, and for roughness, the extent of the spanwise rollup is essential in determining the specific area to be treated. Accordingly, the initial experimental efforts were devoted to flow visualization studies. Three flow visualization techniques were employed-- tufts, paint flow, and photography.

The tufts were used to define the gross flow structure over the model and to provide some guidance for the paint flow application. The tufts were cemented on the hydrofoil in relation to a grid which was penciled onto the foil surface. The tuft flow patterns, which agreed with the paint flow patterns discussed next, indicated the major regions of flow separation.

The paint flow studies provided much more detail of the flow characteristics in the foil boundary layer on the model surface. Several interesting aspects of the flow over the foil are revealed by the paint flow patterns:

(a). A representative flow pattern for the foil pressure side is shown in Figure 13 for design angle of attack $\alpha = 0.5$ deg and $R_c \sim 5 \times 10^6$. With the flow from left to right, note the leading edge of the model. The dark area, where the high local velocities have removed the paint, represents the laminar flow region. Just aft of this region, the ridge of accumulated paint represents laminar separation which is followed by laminar reattachment. Aft of this region the flow is turbulent over the remainder of the foil chord. The approximate transition to chord ratio is $x_t/C \sim 0.06$, indicating that the flow over the foil is almost totally turbulent. Transition data[17] for a 2-D NACA 0018 section at similar conditions gives $x_t/C \sim 0.15$. This is presented only for comparative purposes; obviously, an accurate comparison would require identical geometries and depend upon the rate of amplification of the unstable disturbances and on the intensity of the turbulence in the free stream.

Focusing attention spanwise along the trailing edge in Figure 13, the flow is basically chordwise. However, in the region close to the tip, approximatley 1 in. (0.0254 m) inboard, the flow starts to exhibit an outboard spanwise component which becomes stronger near the foil tip. This spanwise flow is directed into the tip vortex core. Although not shown, the corresponding paint flow for the suction side showed an inboard spanwise component near the tip region, indicating that the suction side tip flow does not enter the tip vortex core.

(b). A paint flow pattern for the foil suction side is shown in Figure 14 for $\alpha = 10$ deg and $R_c \sim 5 \times 10^6$. Again, with the flow from left to right, that although the leading edge laminar-to-turbulent region is similar to that of the $\alpha = 0.5$ deg case, the transition point has moved forward, as expected for the larger angle of attack.
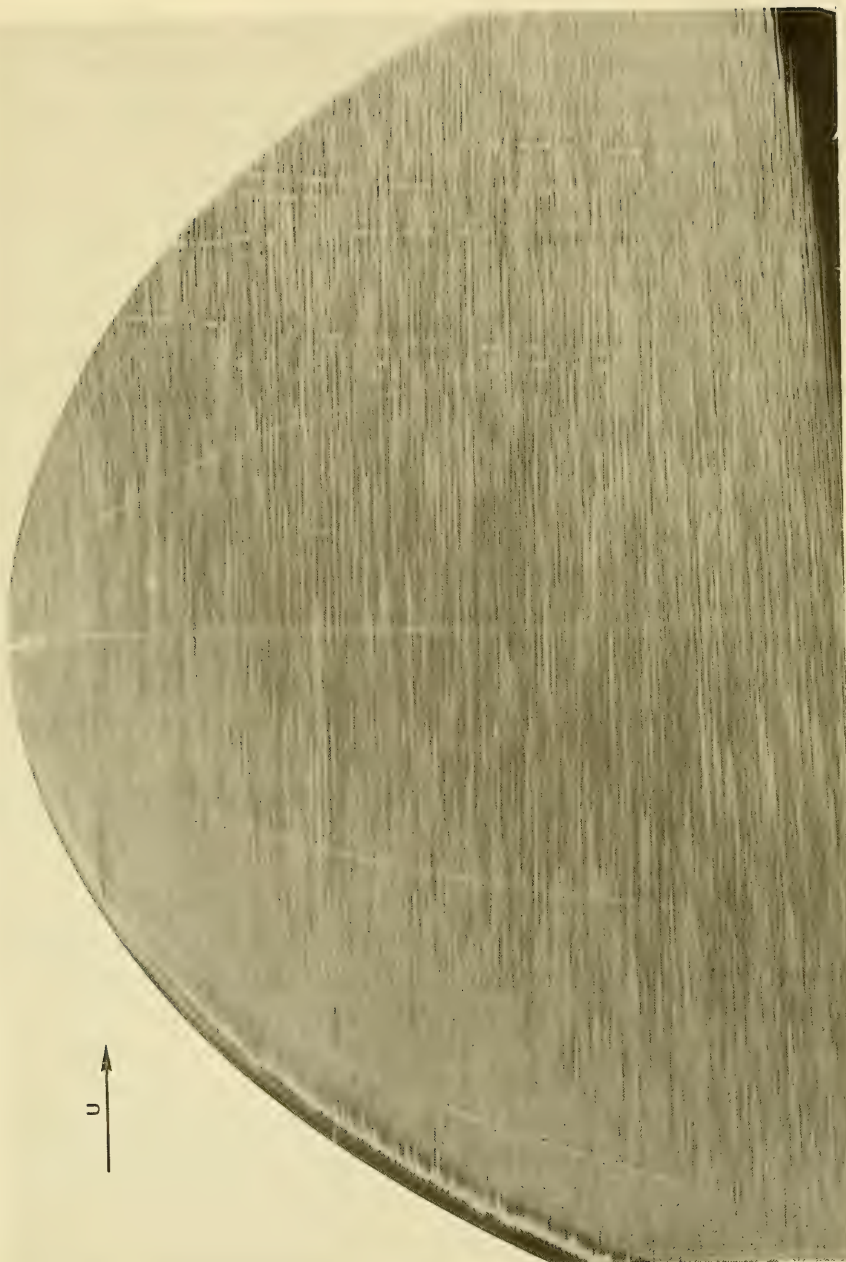
Figure 13 – Paint Flow Pattern—Parent Foil Pressure Side
at $\alpha = 0.5$ Degrees and $R_c = 5 \times 10^6$

U
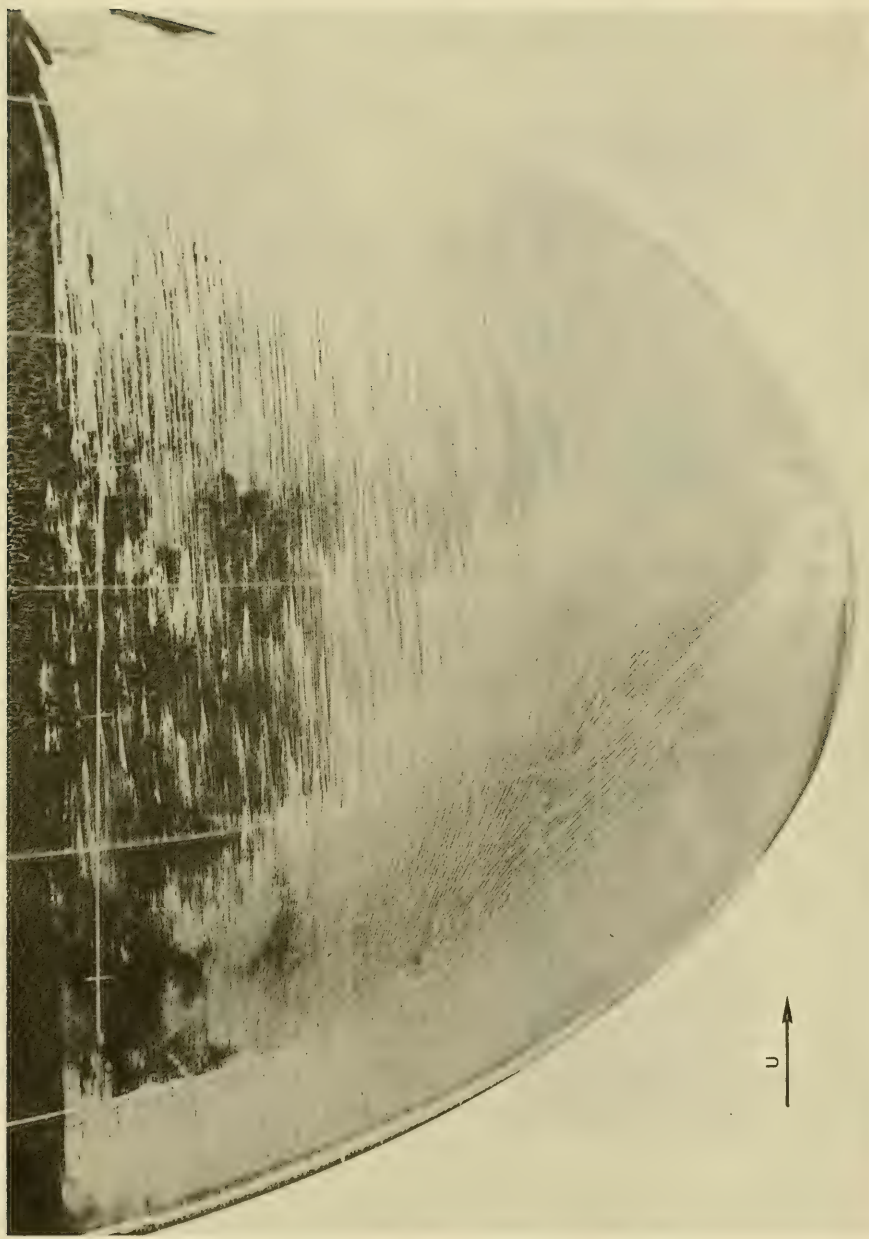
Figure 14 – Paint Flow Pattern—Parent Foil Suction Side
at $\alpha = 10$ Degrees and $R_c = 5 \times 10^6$

U

Also shown in the flow pattern, at approximately 15 percent chord, is a region where there appears to be a strong outward spanwise flow, followed by chordwise flow. This trend was not observed for the smaller α. Inboard along the trailing edge, the area where the paint has failed to migrate or has accumulated represents an area where the flow has separated from the foil surface (a phenomemon that was also observed with the tufts).

Photographs showing the various stages of TVC development are presented in Figure 15. The photographs show the foil suction side at constant α = 10 deg and for R_c and σ as indicated. Figure 15a shows the earlier stages of TVC where the cavitation is primarily limited to the tip vortex wake. This stage also had the tendency to be unsteady with intermittent attachment to the foil tip. For lower σ, Figure 15b shows the vortex attached to the foil tip at approximately midchord. Here, the vortex core diameter has increased and the cavitation is steady and attached. For a more advanced stage, Figure 15c shows the cavitation moving up the foil leading edge with continual increase in the cavitating core diameter. The advanced stage of TVC is shown in Figure 15d where the vortex wake exhibits a marked "twist" and the cavitating vortex has merged with the leading edge cavitation. It should be noted that, in general, during development, the cavitating trajectory down stream of the model does not change and that the attachment point on the foil tip does not move and remains fixed at the tip midchord and just inboard on the foil suction side, independent of α.

Several of the TVC characteristics discussed above were quantified and are presented in Figures 16 and 17. Figure 16 presents the growth of the TVC cavitating core radius as a function of cavitation index σ and angle of attack α and indicates, for fixed α, an approximate exponential increase in core radius as σ decreases from 2.4 to 0.3. For fixed σ, the core radius increases with increasing α. Similar trends have been reported[18] in other TVC studies. The vortex core size was estimated visually by comparison with the foil grid of known widths and spacing. Figure 17 presents the TV trajectory downstream of the foil relative to the foil root. The trajectory was based upon the visual observation documented in Figure 15 and agrees well with the theoretical prediction[19] dealing with the motion of trailing vortices to determine vortex distributions for downwash calculations.

Figure 15a – σ + 3.8, α = 10 Degrees,

$R_c = 2.5 \times 10^6$

Figure 15b – σ = 2.9, α = 10 Degrees,

$R_c = 2.5 \times 10^6$


Figure 15c – σ = 2.0, α = 10 Degrees,

$R_c = 2.5 \times 10^6$

Figure 15d – σ = 1.0, α = 10 Degrees,

$R_c = 3.0 \times 10^6$

Figure 15 – Tip Vortex Cavitation Development--Parent Foil
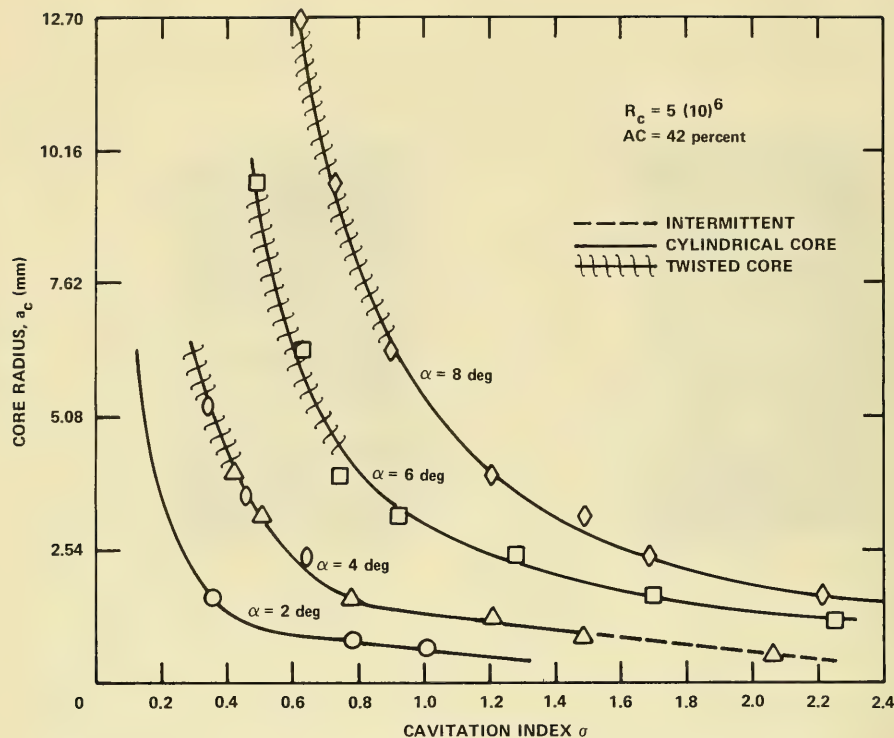
Figure 16 – Core Radius of Cavitating Tip Vortex as a Function of
Cavitation Index σ and Angel of Attack α--Parent Foil
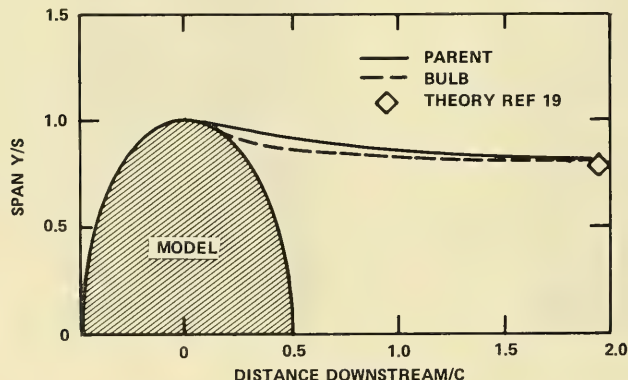

Figure 17 - Tip Vortex Trajectory

FORCES AND TIP VORTEX CAVITATION INCEPTION

The parent foil force characteristics are given in Figures 18 through 20. Figure 18 presents the foil lift coefficient C_L as a function of angle of attack α for Reynolds number R_c = 2.5 and 5.0×10^6. As seen, the results are quite linear over the range of α investigated, -7 deg $\leq \alpha \leq 10$ deg, and agree well with the design theory. The lift curve slope of m = 0.0525/deg α was computed from existing experimental data[16] while the angle of zero lift of α = -2.94 deg and the design angle of attack of α = 0.567 deg were computed from corrected theoretical formulas[20] for two-dimensional NACA a = 0.8 meanline airfoils. The parent foil drag characteristics are given in Figure 19 which shows the variation of drag coefficient C_D as a function of lift coefficient C_L for two Reynolds numbers R_c. In general, the trends observed here are expected; i.e., most of the variation of drag with lift for wings of finite span results from the induced drag, which varies approximately as the square of the lift coefficient for a given wing configuration. The "hump" in the low-drag range is characteristic of the NACA 6-series and results from the sudden shift in boundary layer transition at the end of low-drag range of lift coefficients. In addition, all data for the NACA 6-series wing sections show a decrease of the extent of the low-drag range with increasing Reynolds number.

The roll moment, or the moment due to lift about the root chord, was measured to establish any possible effects of the various foil tip alterations on the spanwise load distribution. The theoretical value for the roll moment arm Yrm can be calculated according to

$$Yrm = \frac{\text{roll moment}}{\text{total lift}} = \frac{\displaystyle\int_o^s \ell Y dy}{\displaystyle\int_o^s \ell dy} = 5.25 \text{ in. } (0.133 \text{ m})$$

or Yrm/s = 0.438

where ℓ = local spanwise load = $\dfrac{c}{2}\left(1 - \left(\dfrac{y}{s}\right)^2\right)^{1/2}$ for elliptic loading.

27

Figure 18 – Lift Coefficient as a Function of Angle
of Attack--Parent Foil

Figure 19 – Drag Coefficient as a Function of Lift Coefficient--Parent Foil
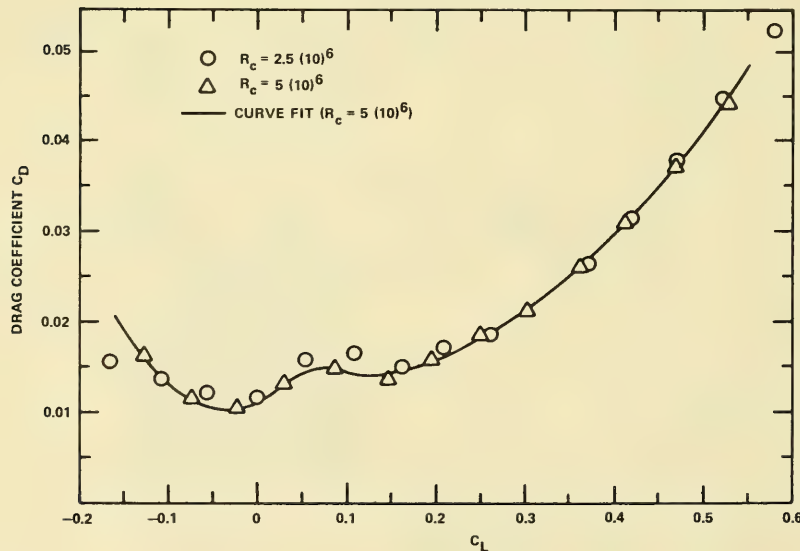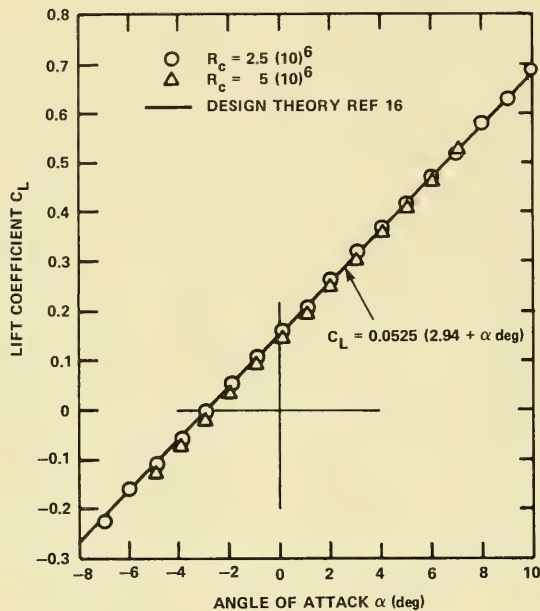
As seen in Figure 20, the experimental roll moment arm data agree well with the predicted value which indicates that the foil develops an elliptic spanwise load distribution as designed.

As discussed earlier, TVC inception was identified as the first appearance of cavitation in the vortex core—usually located approximately one chord length downstream of the foil tip. This procedure offered the best repeatability in identifying this type of cavitation inception. The parent foil TVC inception data are given in Figure 21 and show the variation of cavitation index σ as a function of lift coefficient for Reynolds numbers R_c = 2.5 and 5×10^6. As seen in Figure 21, the parent foil TVC inception data agree well with the form of Equation (1), especially for the C_L range around design. Also, the inception data show a Reynolds number dependence, given as

$$\sigma \sim R_c^{0.36} \tag{2}$$

This Reynolds number dependence agrees with that of McCormick.[4] It is further noted that the inception data are not symmetric about the vertical σ axis. This can be attributed to the favorable chordwise pressure distribution of the cambered foil, at
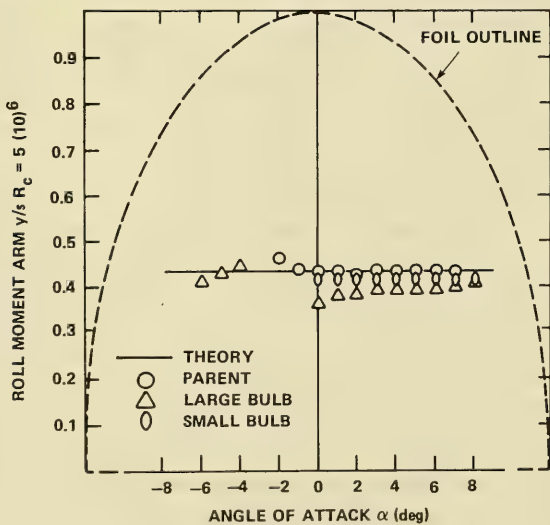
Figure 20 — Roll Moment Arm as a Function of Angle of Attack
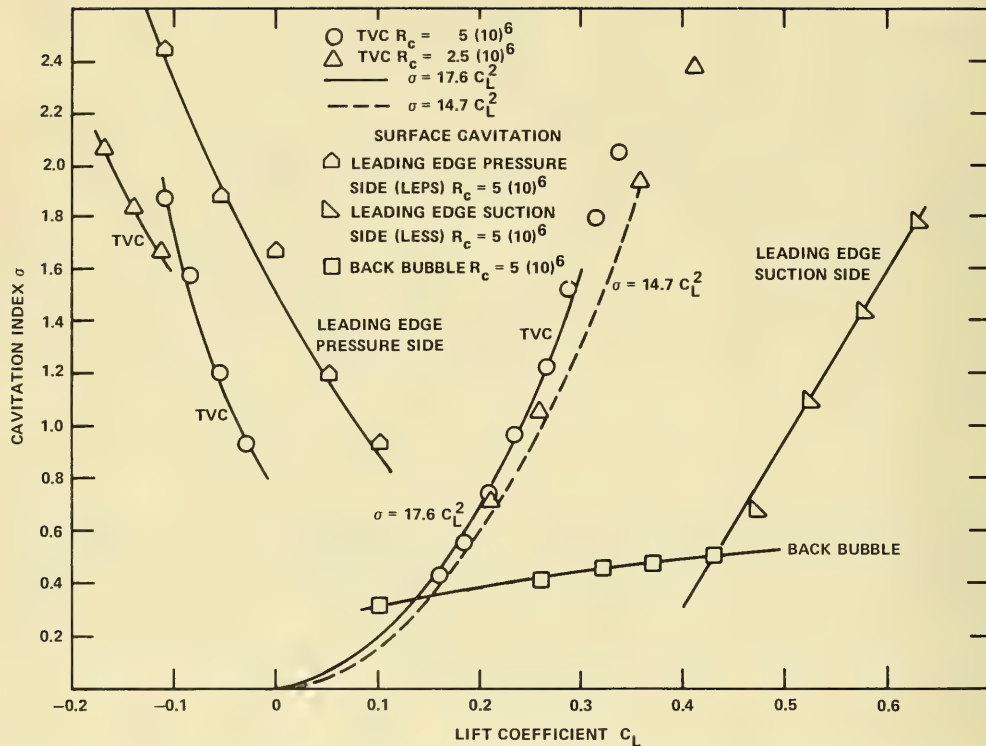
Figure 21 – Cavitation Inception as a Function of Lift Coefficient--Parent Foil

the design condition, which tends to retard the tip vortex rollup process. Also presented in Figure 21 are the cavitation inception data for the various forms of surface cavitation; i.e., leading edge pressure side, leading edge suction side, and back bubble. As seen, TVC is generally the first form of cavitation to appear.

TIP VORTEX CAVITATION DELAY CONCEPTS

Roughened Tip

The use of artifical roughness for TVC delay is a relatively unexplored area. Therefore, the work with this concept was primarily guided by a knowledge of the detailed flow at the foil tip as deduced from the results of the paint flow visualization efforts. In order to avoid substantial increases in drag, the roughness was

applied only to those areas of the foil tip whose streamlines contributed directly
to the forming tip vortex at the foil tip. The paint flow patterns at design α,
(Figure 13) indicated that only the extreme tip area of the foil pressure side--less
than 0.7 percent of the planform area--had to be treated. In addition, the visual
observations--Figure 15--of the TVC revealed that the TV attachment point remained
relatively fixed on the very tip of the foil suction side. On this basis, it was
felt that roughness also applied in this area--less than 0.4 percent of the planform
area--would act in a beneficial manner to reduce the TV core velocities without in-
ducing substantial drag penalties. The roughness grain sizes were large enough to
provide substantial increases in the tip boundary layer thickness, but also were
small enough to avoid local surface cavitation. Since the tip vortex is dependent
upon the tip boundary layer thickness,[4] the roughness size should scale[17] according
to Reynolds number. Figure 8 illustrates the parent foil tip, pressure side, area
which was treated with artifical roughness.

The initial roughness experiments involved the evaluation of the three config-
urations: pressure side only, suction side only and both pressure and suction sides.
A 400-micron grain size roughness was selected and the roughness was applied as dis-
cussed above. The effects of the roughness on pressure and suction sides on the foil
lift and drag were well within the acknowledged 2 percent accuracy of the experiment.
These results are not totally unexpected, considering the relatively small areas that
were treated. Similar force results were obtained for the other two roughness con-
figurations, suction side only and pressure side only.

The cavitation characteristics of the three roughness configurations are pre-
sented in Figure 22. These data correlate well with Equation (1), when compared to
the parent foil, the indicated k values give corresponding increases in TVC inception
speeds of 41 percent for pressure side roughness, 28 percent for suction side rough-
ness, and 67 percent for pressure and suction side roughness. Note that the improve-
ment in cavitation inception for the suction side only and pressure side only rough-
ness appear to be additive. Based upon these results, the optimum roughness pattern
required both pressure and suction side roughness at the tip.

The next phase of the roughness experiments dealt with the optimization of the
roughness grain size. For these experiments the standard or optimum roughness
pattern was used for each of the grain sizes: 90, 400, 600, and 800 microns.
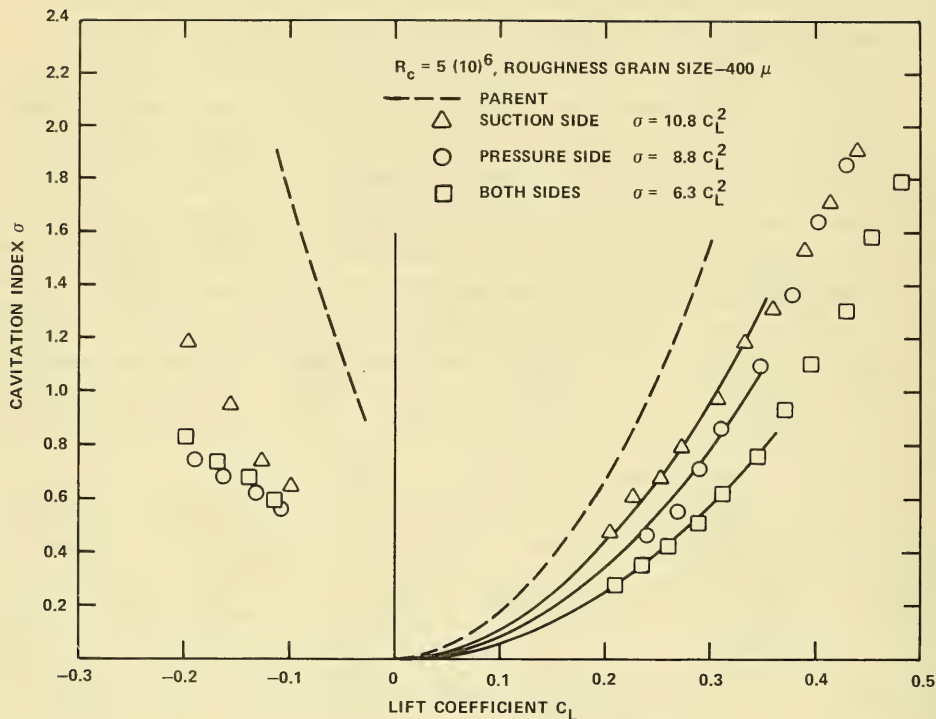
Figure 22 – Cavitation Inception as a Function of Lift Coefficient--
Roughened Foil Tip Pressure Side, Suction Side, and Both
Pressure and Suction Sides--400 Micron

The foil force data indicated that only the 800 micron roughness size introduced a
significant performance penalty--a 5 percent increase in foil drag at design α.

The TVC inception data for the various roughness sizes are shown in Figure 23.
These data indicate, for each roughness, substantial improvement in TVC performance
over a wide range of C_L. In general, TVC performance improves--lower σ--as the
roughness size increases. Also, the differences between the 600- and 800-micron
data are small, which could represent a limiting roughness size for these particular
experimental conditions. In order to make a better comparison of foil performance
in terms of TVC due to variations in roughness, per se, the grain size data are
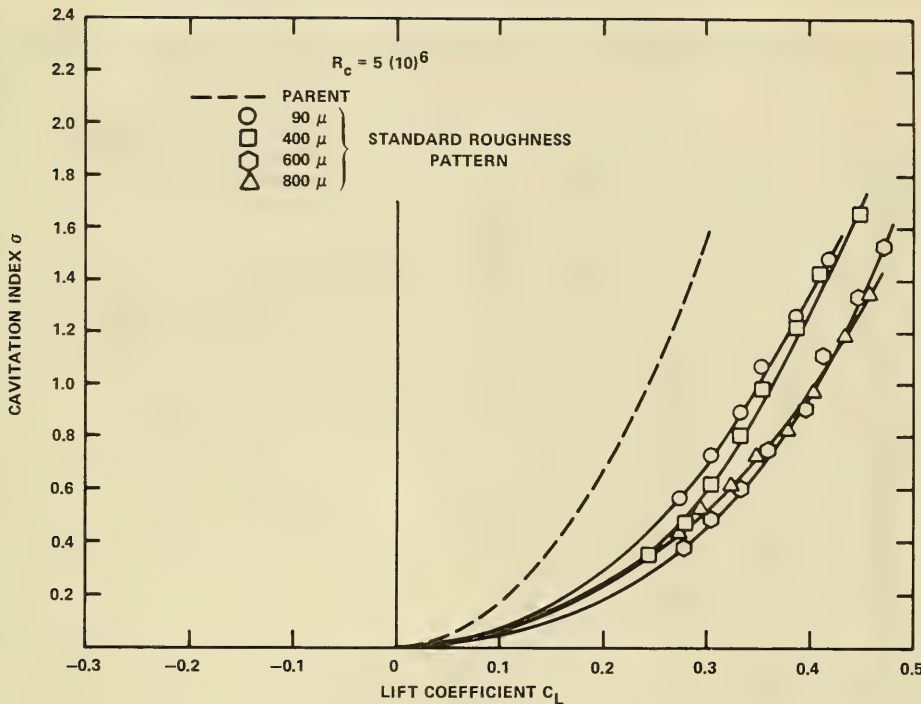
Figure 23 – Cavitation Inception as a Function of Lift Coefficient
for Varying Roughness Grain Size--Standard Roughness Pattern

presented in Figure 24 to show the relative increase in TVC inception speed relative
to the parent foil, over a range of C_L. The relationship between σ and U is obtained
directly from the expression

$$\sigma = \frac{P_\infty - P_v}{\frac{1}{2}\rho U^2}$$

and for constant $(P_\infty - P_v)$

$$\frac{U_\beta}{U_p} = \left(\frac{\sigma_p}{\sigma_\beta}\right)^{1/2}$$
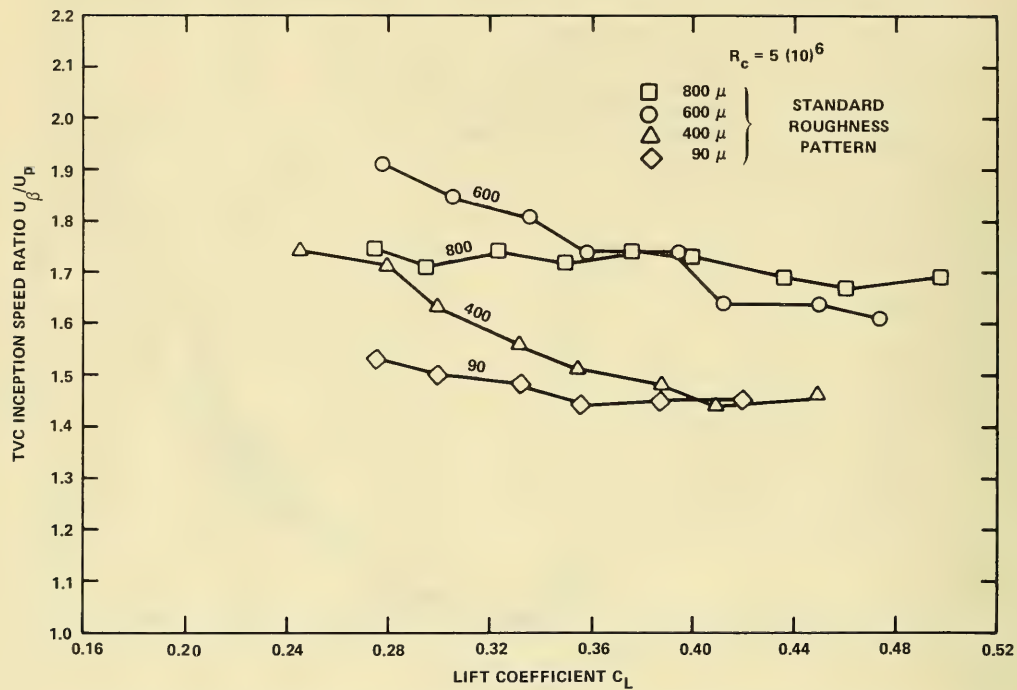
Figure 24 – Tip Vortex Cavitation Inception Speed Ratio as a Function of Lift
Coefficient for Varying Roughness Grain Size--
Standard Roughness Pattern

where the subscripts β and p refer to the altered and parent foils, respectively.
The data in Figure 24 exhibit the following trends:

   (a).   Each of the roughness grain sizes produces significant increases in the
TVC inception speed; e.g., for $C_L \sim 0.28$, 53 percent for 90 micron, 71 percent for
400 micron, 92 percent for 600 micron, and 74 percent for 800 micron.

   (b).   In general for a fixed roughness size, the effectiveness of roughness is
reduced for the higher α; i.e., for each grain size, U_β/U_p decreases as C_L increases.
Apparently the ability of the roughness to dissipate or destablize the tip vortex
core energy is reduced as the tip vortex vorticity is increased, i.e., increased C_L.

(c). The 600-micron grain size appears to be the most effective; e.g., for angles of attack close to design, $0.28 \leq C_L \leq 0.36$, the 600-micron size produced substantially larger values of U_β/U_p as compared to the other grain sizes.

The roughness suction side surface cavitation inception data are given in Figure 25 for the standard roughness pattern. These data were recorded for the first appearance of cavitation on the distributed roughness and were generally associated with a localized nonuniformity which resulted during the application of the roughness. A more uniform application of the roughness should result in lower σs for all the grain sizes. For the foil suction side tip, the trends are as expected and show that the larger grain sizes result in higher σ values or lower cavitation inception
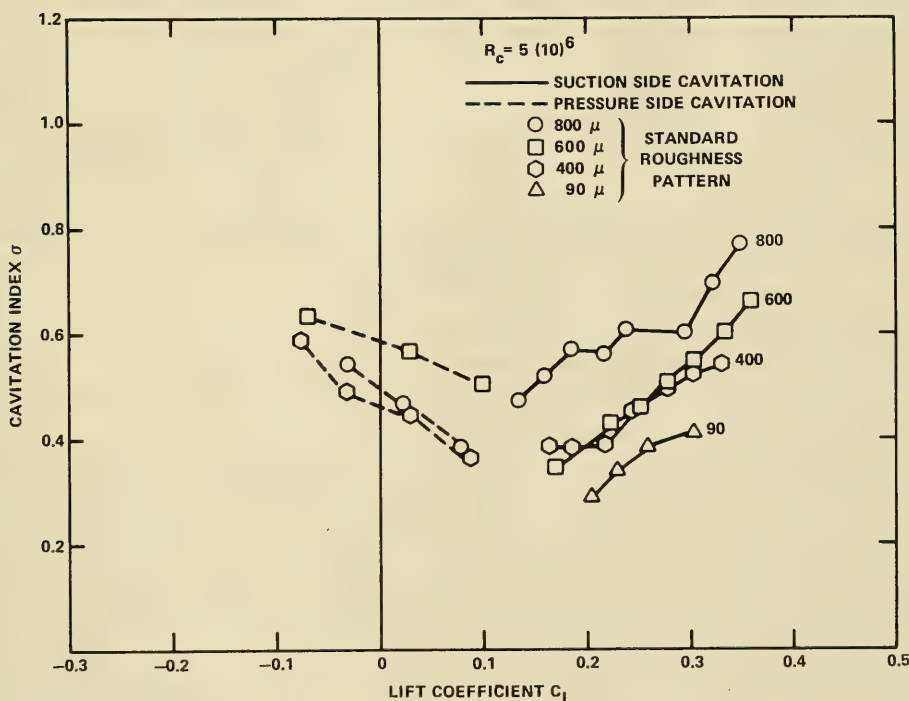

Figure 25 - Surface Cavitation Inception as a Function of Lift
Coefficient for Varying Roughness Grain
Size--Standard Roughness Pattern

speeds. For the smaller grain sizes, (90 and 400 micron), the surface inception data indicate lower σs or higher inception speeds as compared to the corresponding TVC inception data. However, for the larger grain size (600 and 800 micron), the surface cavitation inception numbers approach or exceed the corresponding TVC inception numbers. This may not pose any problems because recent studies[21] have shown that distributed surface roughness cavitation is weekly dependent upon Reynolds number while the TVC is strongly Reynolds number dependent. On this basis, a qualitative statement can be made that, for higher Reynolds number, surface roughness cavitation would appear at lower σ or higher inception speeds as compared to TVC. However, it should be emphasized that the referenced work[21] is somewhat limited in scope; i.e., essentially flat plate--zero pressure gradient--conditions at relatively low Reynolds numbers with wire screen roughness. Additional research will be required before this issue can be better quantified.

Based upon the above discussion and the data presented in Figures 22-25, the 600-micron grain size roughness appears to be the optimum grain size for these experimental conditions. The 600-micron grain size resulted in the largest TVC inception speed increase of 92 percent with no loss in foil performance--no drag increase or lift decrease.

The final phase of the roughness experiments involved two efforts. The first effort dealt with an attempt to improve the TVC performance by increasing the treated area of the foil pressure side. For this experiment, the 600-micron grain size was applied to the area 0.75 in. (0.019 m) inboard from the tip, corresponding to an area of approximately 1.8 percent of the total pressure side area. This treatment represented an area approximately twice that of the standard which represented the area 0.5 in. (0.013 m) inboard from the tip. The suction side area was kept the same as the standard with 600-micron grain applied to the area 0.25 in. (0.006 m) inboard from the tip. The foil performance with the increased treated area indicated an increase in foil drag of approximately 4 percent over that of the standard. The corresponding TVC inception data, shown in the upper two curves of Figure 26, indicated a slight increase in U_β/U_p compared to the standard pattern. These slight increases in TVC performance are not considered significant in light of the increased drag penalty, and the "standard" configuration is taken to be the optimum roughness pattern. The second effort involved an attempt to improve the 600-micron standard
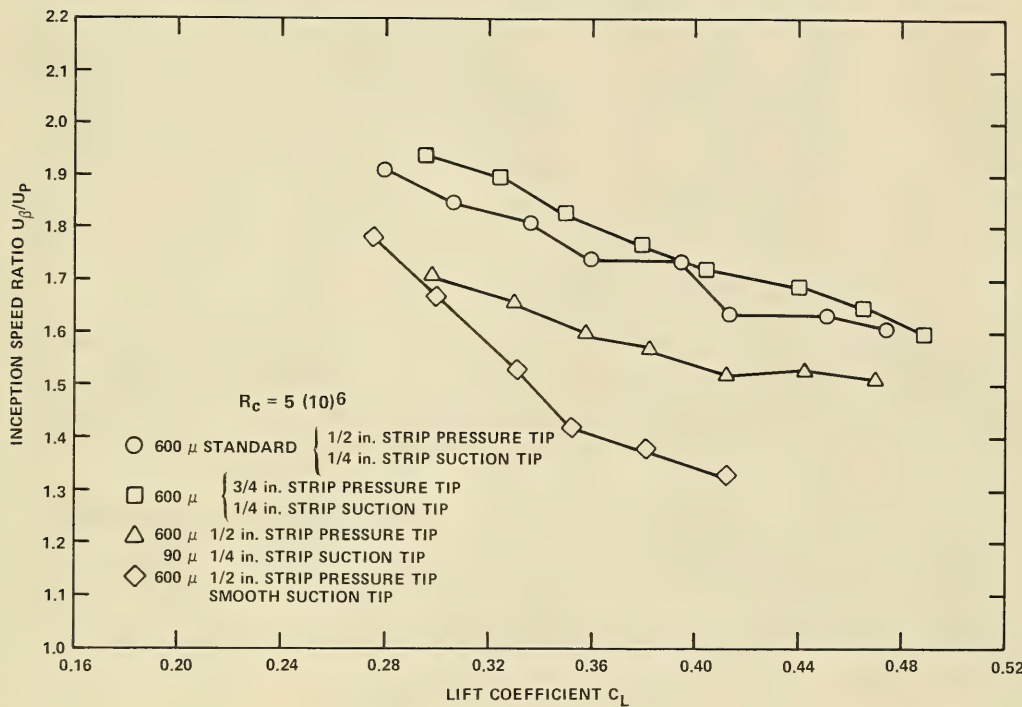
Figure 26 – Tip Vortex Cavitation Inception Speed Ratio as a Function of Lift
Coefficient for Increased Roughness Treated Area
and Reduced Suction Side Roughness Grain Size

suction side surface cavitation characteristics. For this effort, the standard pat-
tern was used with 90-micron grain size on the suction side tip and 600-micron grain
size on the pressure side tip. As seen in Figure 26, this arrangement resulted in
substantial reductions in U_β/U_p as compared to the same distribution with 600-micron
on both the suction and pressure sides. Although the 90-micron/600-micron arrange-
ment improves the surface cavitation characteristics as compared to the 600-micron/
600-micron arrangement (Figure 25), this grain is negated by the corresponding loss
in TVC performance.

Before concluding the roughness discussion, it may prove useful, with regard to scaling, to compare the foil tip boundary layer thickness δ with the roughness height k_s. The detailed calculation is given in the Appendix and assumes fully turbulent flat plate flow with zero pressure gradient. For the experimental conditions reported, U = 43 ft/sec (13.1 m/sec) and k_s = 600 microns, the ratio of roughness boundary layer thickness δ_r to the roughness height (grain size) k_s is estimated to be

$$\delta_r/k_s \sim 0.38$$

or a roughness height approximately 40 percent of the boundary layer thickness. This calculation is presented for comparative purposes only; obviously the flat plate assumption will overpredict δ_r at the hydrofoil leading edge. The scaling implications involving the boundary layer parameters and k should be the subject of further research.

In summary, the roughness experiments identified an optimum roughness pattern and grain size-600-micron grain size applied to both the pressure and suction side tips as prescribed above. This particular roughness arrangement resulted in TVC inception speed increases of up to 92 percent with no measurable loss in foil performance.

Bulbous Tip

As discussed earlier, the bulb modification involved only the thickening of the cambered airfoil sections of the parent foil in order to minimize both performance loss and local surface cavitation. The maximum bulb thickness was based upon the findings of Crump.[13] The experimental lift curve slope data for the large and small bulbous tip foil are shown in Figure 27 and indicate a loss of 7.5 and 2.9 percent in the lift curve slope respectively as compared to the parent foil. Additional insight also is given in Figure 20, which shows that the roll moment arm for the bulbous tips has moved inboard approximately 6.6 and 2.5 percent of the foil span for the large and small bulbs respectively. This result is shown qualitatively in Figure 17 which indicates that the spanwise location of the bulb TVC has moved inboard. These combined results indicate that the bulb sections are not producing the predicted lift. This loss was somewhat unexpected since the bulb was initially designed to have a lift curve slope similar to the parent--lifting surface theory
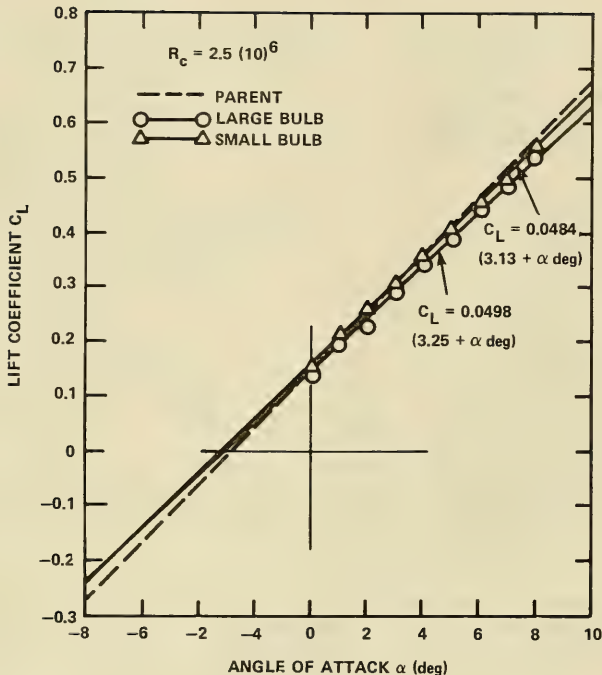
Figure 27 – Lift Coefficient as a Function of Angle
of Attack--Bulbous Tip Foils

predicted comparable lift curve slopes since the only difference was the spanwise
thickness distribution. In addition, wingtip bulbs are known[22] to behave similarly
to endplates which retard the rollup process, resulting in an effective increase in
the lift curve slope. The bulb drag data are given in Figure 28 and show a 6.9 and
13.2 percent increase in drag at the design C_L for the small and large bulb respec-
tively. The larger drag increases for larger C_L reflects the change in the lift
curve slope. These observed drag increases are significant and are apparently
related to both the increased bulb surface area and the profile drag.

The cavitation characteristics of the bulbous tip foils are shown in Figure 29.
As seen, Equation (1) fits the data quite well, e.g., the large bulb data indicate
$k \sim 9.9$, which corresponds to a 33 percent increase in the TVC speed as compared to

39
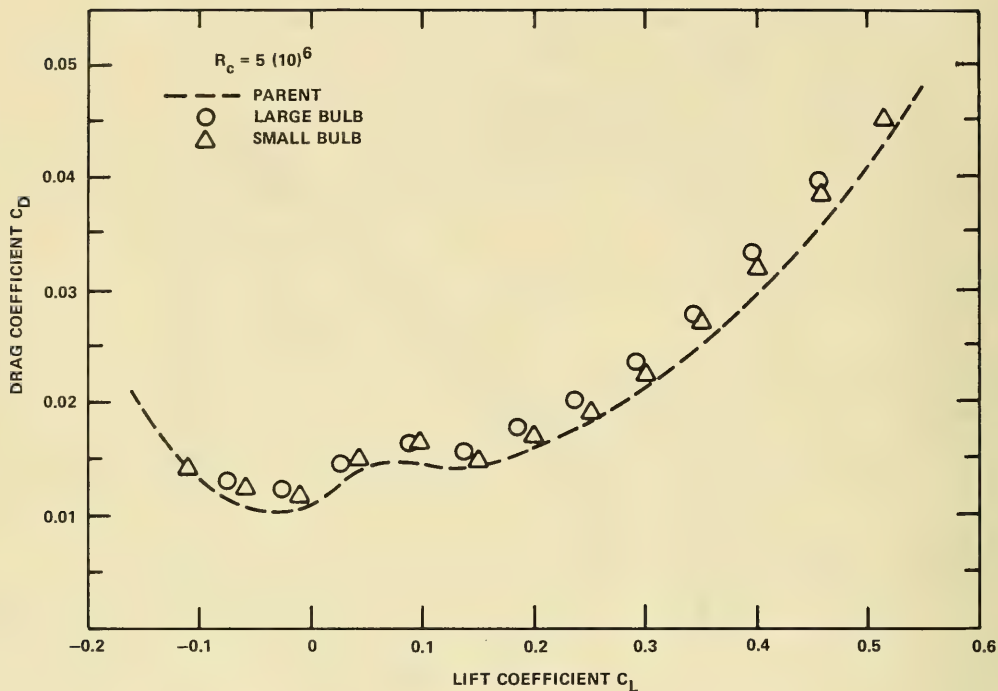
Figure 28 – Drag Coefficient as a Function of Lift
Coefficient--Bulbous Tip Foils

the parent. The small bulb is somewhat less effective. The appearance of the bulb
TVC was similar to that of the parent; however, the location was different (as dis-
cussed above and shown in Figure 17).

For the parent foil, the cavitation data were limited for the low σ values due
to tunnel saturation conditions. However, this was not the case for the bulbous
tips. Here, the lowest σ value for each bulb represented a threshold above which
TVC was not observed. Also shown in Figure 29, the bulbs did induce some local sur-
face cavitation--back bubble cavitation--which was attributed to the relatively large
thickness/chord ratios of the bulb sections made necessary by the short chord lengths
at the foil tip.
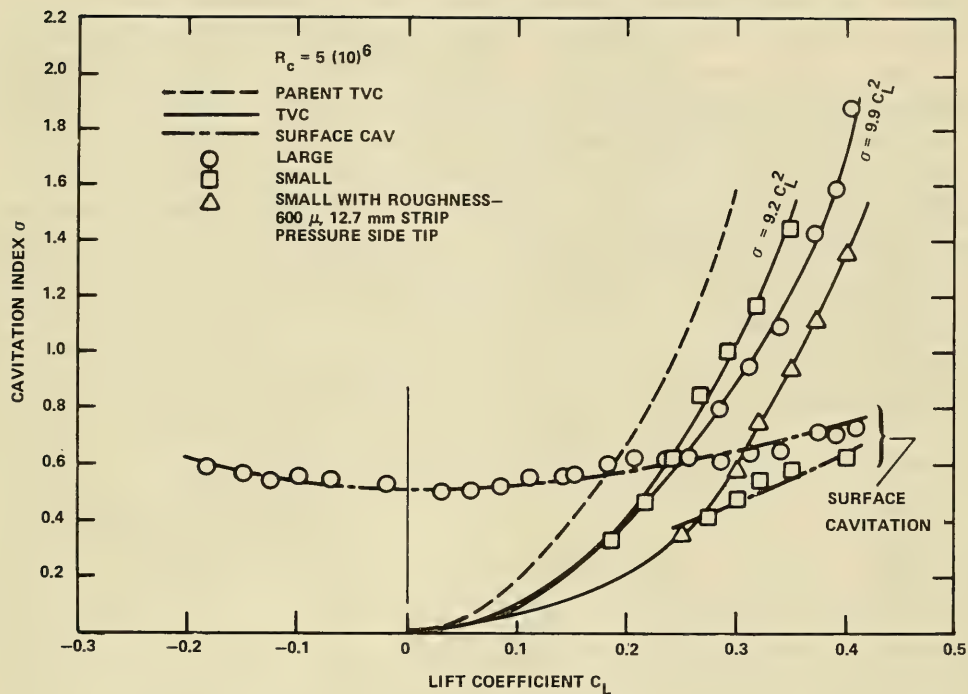
Figure 29 – Cavitation Inception as a Function of Lift
Coefficient--Bulbous Tip Foils

A bulb with roughness was also evaluated. For this experiment, 600-micron
roughness was applied to the small bulb pressure side tip over the area 0.5 in.
(0.013 m) inboard from the bulb tip. As seen in Figure 29, this configuration
resulted in substantial improvement in TVC performance as compared to the bulb with-
out roughness. These data indicate that the roughness is also effective in delaying
TVC for configurations with unloaded tips.

The bulb data are also presented, Figure 30, to show the relative increase in
TVC inception speed over a range of C_L. As seen, the larger bulb gives increased
TVC inception speeds of from 10-15 percent higher than the smaller bulb.

However, this small increase in TVC performance is also accompanied by a drag
increase approximately double that of the smaller bulb. On this basis, the smaller
bulb appears to be the more acceptable bulb shape. The data for the small bulb with
roughness show substantial increases in TVC inception speed for the lower values of
C_L. However, U_β/U_p falls off rather rapidly for the larger C_L values. This trend
is also present in the data for the roughness alone (no bulb) in Figure 26. In
addition, comparison of the data for the bulb with roughness and the corresponding
data for roughness alone (Figure 26--diamond symbols) show that, for C_L < 0.32, the
bulb provides no substantial increases in U_β/U_p. However, for C_L > 0.32, the bulb
provides an additional 10 percentage points in U_β/U_p.
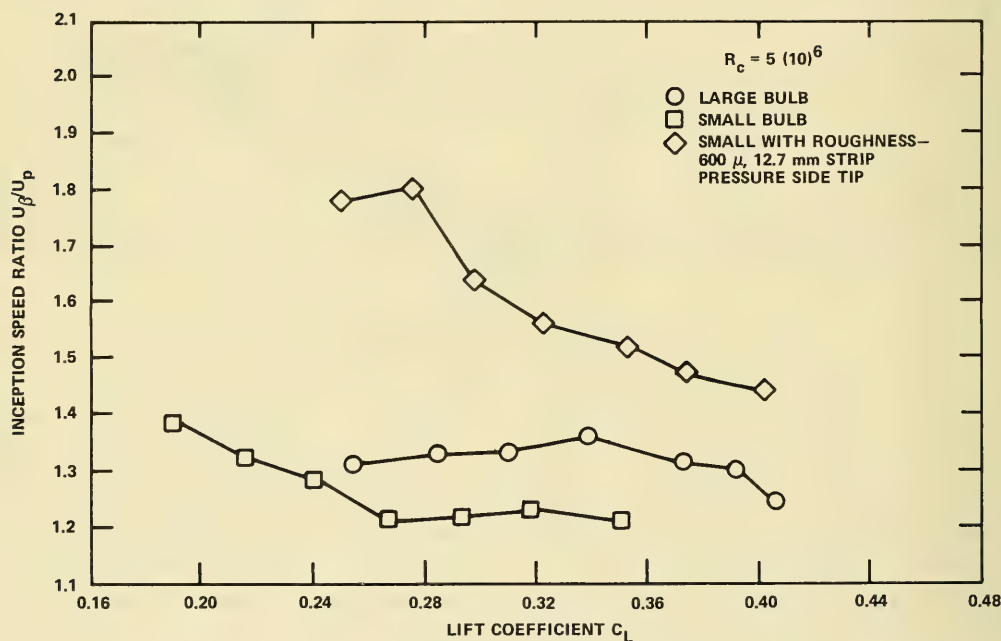
Figure 30 – Tip Vortex Cavitation Inception Speed Ratio as a Function
of Lift Coefficient for the Bulbous Tip Foils

Passive Mass Injection Tip

Passive Mass Injection (PMI) is a new concept and again, as in the case of the roughness, the design was guided primarily by a basic knowledge of the tip flow. This TVC delay mechanism is governed by the viscous interaction of the fluid flow exiting from the PMI channel with the tip vortex flow. The mass flow through the channel is dependent upon the differential pressure between the entrance and exit of the channel, including the effective component of free stream stagnation pressure. The channel exit was located on the tip suction side at the observed attachment point of the tip vortex--Figure 15--and aligned with the vortex core. The entrance of the PMI channel was located on the tip pressure side to align the channel, within the physical constraints of the foil tip geometry, with the free stream in such a manner as to maximize the channel mass flow. Two channel diameters were investigated, PMI 1--0.125 in. (3.2 mm) and PMI 2--0.188 in. (4.8 mm).

The effects of the PMI channels on the foil lift and drag were well within the experimental accuracy. Again, this result is expected, considering the small size of the channels.

The cavitation characteristics of the PMI foil are given in Figure 31. For the PMI 1 and the lower values of C_L, $C_L \leq 0.2$, the data indicate that the PMI offers no improvement--the TVC inception data coincide with that of the parent foil. However, for larger C_L, $C_L > 0.2$, the data show that the PMI is effective and the data again agree with Equation (1) for k = 14.1, representing an increase in the TVC inception speed of 12 percent relative to the parent. These results indicate that, for this channel configuration, the mass flow through the channel is insufficient for C_L < 0.2. The low σ conditions for the PMI 2 were not achieveable; but as C_L increases, the PMI 2 performance improves as compared to PMI 1. This indicates that PMI 2 provides larger mass flows into the vortex core as expected. The results from Figure 31 also show some local cavitation associated with the PMI channels; for C_L ≤ 0.2, this cavitation was located inside the PMI channels and for $C_L > 0.2$, the cavitation initiated at the downstream edge of the channel exit, on the foil suction side. This problem may possibly be alleviated through refinements in the channel geometry.

The PMI was also evaluated with roughness. For this investigation, as with the bulb, 600-micron roughness was applied to the PMI 2 pressure side tip over the area
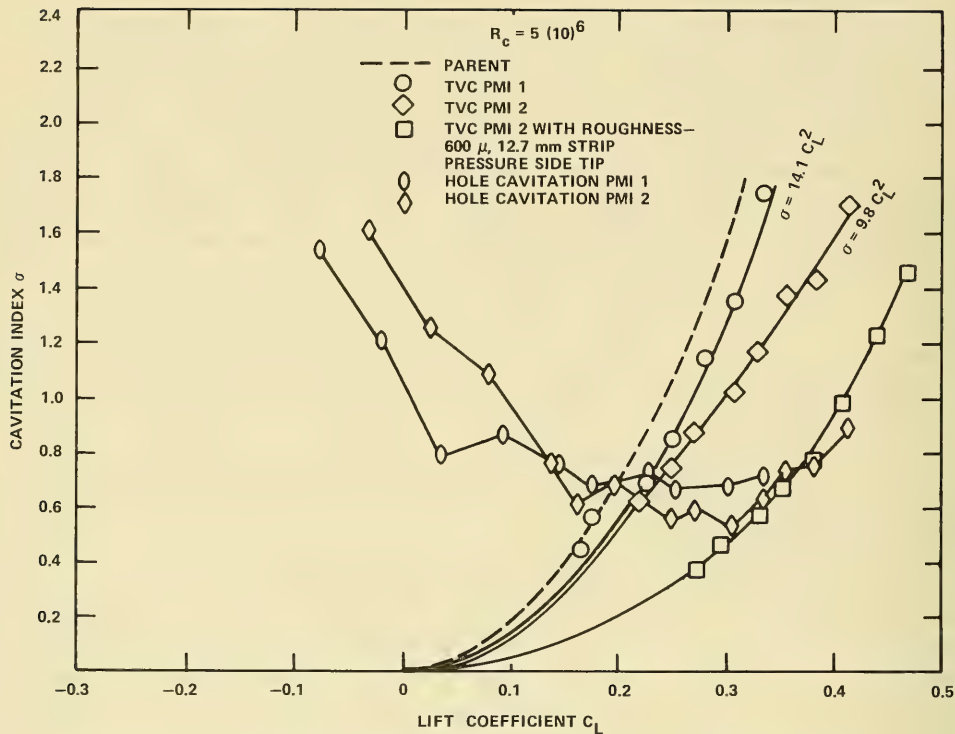
Figure 31 – Tip Vortex Cavitation Inception as a Function of Lift
Coefficient--Passive Mass Injection Foil

(excluding the channel area) 0.5 in. (0.013 m) inboard from the foil tip. As seen
in Figure 31, this configuration resulted in substantial improvement in TVC perform-
ance as compared to PMI 2 without roughness.

The PMI data are also presented in Figure 32 to show the relative increase in
TVC inception speed over a range of C_L. The data trends are basically as discussed
above (for increasing C_L the PMI 1 becomes less effective, indicating an insufficient
mass flow into the vortex core, while the PMI 2 shows a steady increase in perform-
ance due to the larger mass flows associated with the larger channel). PMI 2 is the
largest size channel which could be physically accommodated in the foil tip.
However, these trends indicate that TVC performance increases with increasing PMI
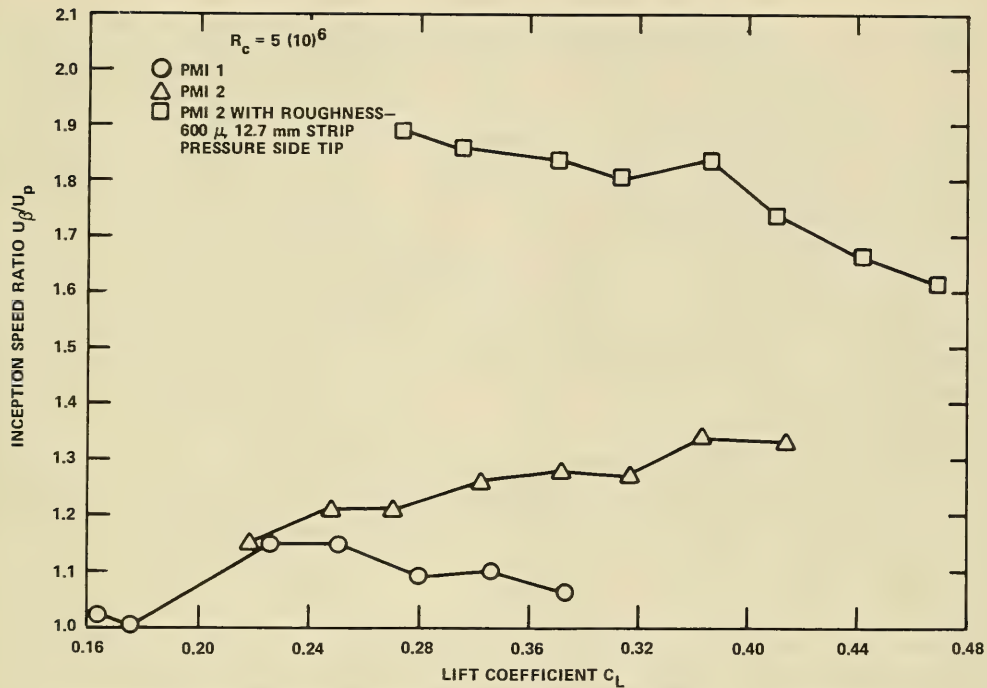
Figure 32 – Tip Vortex Cavitation Inception Speed Ratio as a Function of
Lift Coefficient for the Passive Mass Injection Foil

channel size. The optimum PMI channel size would have to be determined on a model
with sufficient tip thickness. The data for the PMI 2 with roughness show sub-
stantial increases in the TVC inception speed as compared to the PMI 2 without
roughness. Comparsion of the data for PMI 2 with roughness (Figure 32) and the
corresponding roughness alone (Figure 26 diamond symbols) show that the individual
performance gains are approximately additive.

Active Mass Injected Tip

As discussed previously, the principles governing the Active Mass Injected
(AMI) and PMI tips are similar, the only difference being that the AMI mass flow
rates into the vortex core are augmented by an external energy source. The end of
the AMI tube was located in the tip of the foil suction side at the observed

45

attachment point of the tip vortex (Figure 15) and aligned streamwise with the vortex core. The designed AMI delivery rates were based upon tip vortex mass injection data[14] obtained in wind tunnel experiments. The data from these experiments indicated optimum injection velocities U_i for vortex wake dissipation to be approximately three times that of the free stream velocity 3U. For this study, with U ~ 43 ft/sec (13.1 m/sec) and an injection tube ID = 0.104 in. (0.0034 m), the maximum AMI designed delivery rate was 3.42 gal/min (12.95 ℓ/min).

The AMI had no measurable effect on the foil lift over the range of delivery rates Q investigated--0.3 to 2.4 gal/min (1.14-9.08 ℓ/min). For the higher delivery rates, the foil drag was decreased approximately 10 percent as expected, due to the AMI jet reaction force.

The cavitation characteristics of the AMI are given in Figure 33. These data show the following trends:

(a). Each of the AMI delivery rates shows significant increases in the TVC inception speed U_β/U_p over the entire range of C_L investigated; e.g., for design C_L ~ 0.2, a Q ~ 1.2 gal/min (4.54 ℓ/min) resulted in a 53 percent increase in TVC inception speed.

(b). In general, U_β/U_p increases with increasing Q up to Q ~ 1.2 gal/min (4.54 ℓ/min), where further increases in Q--up to Q ~ 2.4 gal/min (9.08 ℓ/min)--show no appreciable increase in U_β/U_p.

(c). For the lower Q, Q ~ 0.3 and 0.6 gal/min (1.14 and 2.27 ℓ/min), U_β/U_p decreases rapidly with increasing C_L. As was the case for the roughness, apparently the lower injection rates are not sufficient to dissipate or destablize the tip vortex core energy for the higher tip vortex vorticity--higher C_L. The higher Q--Q ~ 0.9, 1.2, and 2.4 gal/min (3.41, 4.54, and 9.08 ℓ/min)--did not suffer in this respect and, in general, were equally effective over the whole range of C_L investigated.

(d). The AMI data (Figure 33) can be used to estimate the mass delivery rates produced by the PMI (Figure 32). Comparing Figures 32 and 33 over the range of parameters $1.2 < U_\beta/U_p < 1.3$ and $0.24 < C_L < 0.36$, one sees that the PMI 2 produced mass flow rates into the tip vortex core of from approximately 0.3 to 0.9 gal/min (1.14 to 3.41 ℓ/min).

Based upon these observations, the optimum AMI mass flow rate is seen to be Q ~ 1.2 gal/min (4.54 ℓ/min). It is interesting to note that this mass flow rate is
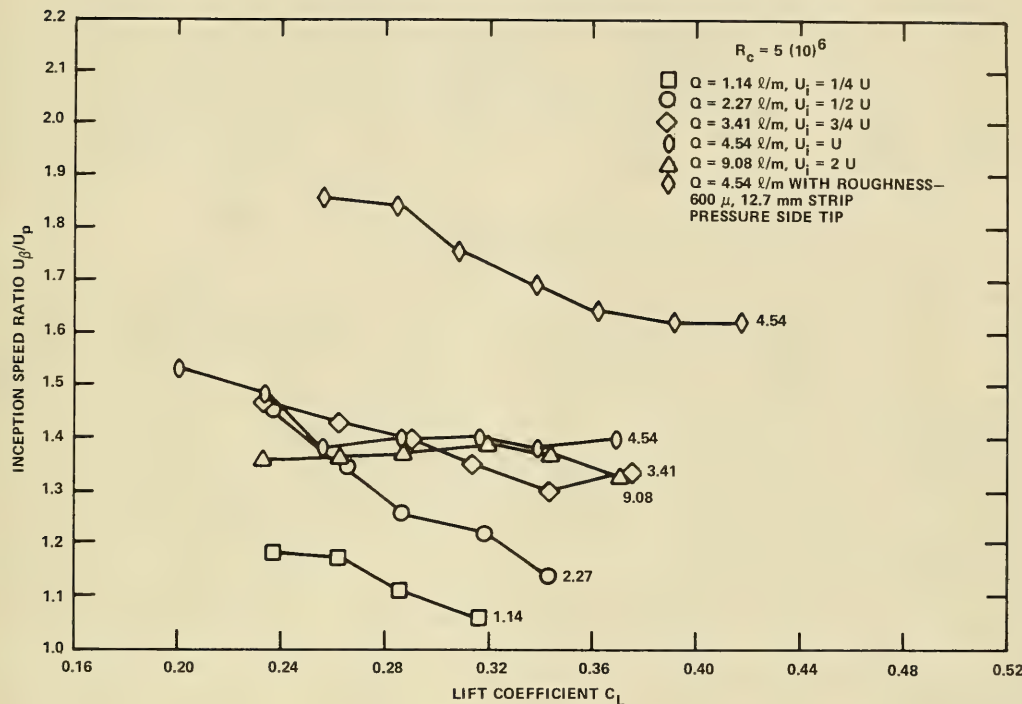
Figure 33 – Tip Vortex Cavitation Inception Speed Ratio as a Function of Lift Coefficient for the Active Mass Injection Foil

approximately equivalent to the flow rate obtained using an average injection velocity U_i equal to the freestream velocity U, $U_i = U$, and area based on the injection nozzel inside diameter.

SUMMARY AND CONCLUSIONS

Several TVC delay concepts have been evaluated at high Reynolds number on a three-dimensional lifting surface. The results indicate that all of the concepts significantly delay TVC inception: increased TVC inception speeds of 94 percent for the roughened tip, 38 percent for the bulbous tip, and 33 and 54 percent for the passive and active mass injection tips, respectively. In most cases, the

improvements in TVC inception were accomplished with a minimal decrease in the lifting surface performance. In addition, the parent foil cavitation inception data scale with Reynolds number according to $\sigma \sim R_c^{0.36}$ and also agree well with the relation $\sigma = k \, C_L^2$. A summary of the results for the optimum TVC delay concepts are given in Table 1.

<div align="center">
TABLE 1 - SUMMARY OF RESULTS FOR THE OPTIMUM TIP VORTEX
CAVITATION DELAY CONCEPTS
</div>

	Parent	Roughness 600 μ Pressure and Suction Side Tip	Bulb Small	Passive Mass Injection 2	Active Mass Injection $Q_i = 4.54$ ℓ/m
Lift Coefficient Slope, m	0.0523	0.0530	0.0513	0.0531	0.0523
Δm	-	1.3 percent*	-2.0 percent	1.5 percent*	0*
Drag Coefficient C_D at Design C_L	0.0159	0.0159	0.0170	0.0161	0.0144
ΔC_D	-	0.0 percent*	6.9 percent	1.3 percent*	-9.4 percent
Inception Curve Constant K	17.6	4.8	9.2	9.8	7.5
Inception Speed Ratio U_β/U_p Parent	1.00	1.91	1.38	1.34	1.53
*Within experimental accuracy.					

The flow visualization techniques employed in this study proved effective in defining the detailed flow over the model hydrofoils and also provided the design criteria for the various TVC delay concepts. The paint flow experiments indicated that the flow over the hydrofoils was almost totally turbulent for the investigative Reynolds number $R_c \sim 5 \times 10^6$.

Although all of the concepts evaluated significantly improved TVC performance, the roughened tip proved, by far, to be the superior. Thus, continued work in this area should first be directed to the roughened tip. In particular, the current study should be exteneded to higher Reynolds numbers; and also, for scaling purposes, cover a broader range of Reynolds number. In addition, the effects of roughness on surface cavitation should be given close attention.

APPENDIX

HYDROFOIL TIP BOUNDARY LAYER THICKNESS AND ROUGHNESS HEIGHT

To compare the foil tip boundary layer thickness δ with the corresponding rough-
ness height (grain size) k_s, assume that the tip flow is similar to fully turbulent
flat plate flow with zero pressure gradient shown below.
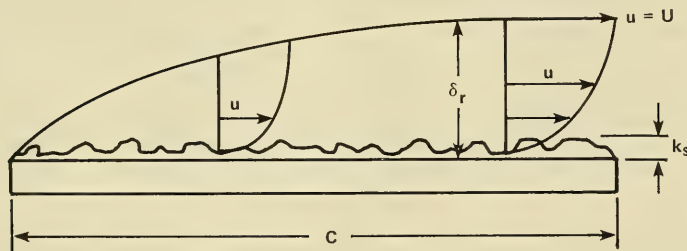
Figure 34 – Schematic Diagram of a Turbulent Boundary Layer on a Rough Wall

The Reynolds number, based on a representative tip chord length c of 2 in. (0.051 m)
and a free stream velocity U of 43 ft/sec (13.1 m/sec) is

$$R_c = Uc/\nu = 8.3 \times 10^5$$

The corresponding boundary layer thickness for the smooth tip δ_s is given as[23]

$$\frac{\delta_s}{x} = \frac{0.0598}{\log R_c - 3.17} = 2.2 \times 10^{-2}$$

or for $x = c = 2$ in. (0.051 m)

$$\delta_s \sim 0.044 \text{ in. } (0.0011 \text{ m})$$

and for the 600-micron grain size k_s, this gives

$$k_s/\delta_s \sim 0.54$$

The corresponding boundary layer thickness for the roughened tip δ_r can be estimated as follows. In the completely rough regime, the local coefficient of skin friction C_f is related to the roughness height k_s according to the equation[17]

$$C_f = [2.87 + 1.58 \log (x/k_s)]^{-2.5}$$

which, for $x = c = 2.0$ in. (0.051 m) and $k_s = 0.024$ in. (600 μ) gives

$$C_f = 0.0118$$

The boundary layer thickness δ_r follows from the relation[24]

$$C_f^{-1/2} = 3.96 \log (\delta_r/k_s) + 7.55$$

and for $C_f = 0.0118$ and $k_s = 0.024$ in. (600 μ)

$$k_s/\delta_r \sim 0.38$$

REFERENCES

1. Platzer, G.P. and W.G. Souders, "Tip Vortex Cavitation Delay with Application to Marine Lifting Surfaces--A Literature Survey," DTNSRDC Report 79/051 (Aug 1979).

2. Lamb, H., "Hydrodynamics," Cambridge (1932).

3. Corsiglia, V.R. et al., "Rapid Scanning, Three-Dimensional Hot Wire Anemometer Surveys of Wing-Tip Vortices," J. Aircraft, Vol. 10, No. 12, pp. 752-757 (Dec 1973).

4. McCormick, B.W., Jr., "On Cavitation Produced by a Vortex Trailing from a Lifting Surface," J. Basic Engineering, pp. 369-379 (Sep 1962) (extends Ph.D. Thesis, Pennsylvania State University, 1954, to Larger Reynolds numbers).

5. Grow, T.L., "The Effect of Wing Geometry and Lower Surface Boundary Layer on the Roll-Up Tip Vortex," M.S. Thesis, Penn. State University (June 1967).

6. Batchelot, G.K., "Axial in Flow in Trailing Line Vortices," J. Fluid Mech., Vol. 20, Part 4, pp. 645-658 (1964).

7. Moore, D.W. and P.G. Saffman, "Axial Flow in Laminar Trailing Vortices," Proc. Royal Soc. London A. 333, pp. 491-508 (1973).

8. Bryant, L.W., "An Investigation of the Flow of Air Around an Aerofoil of Infinite Span," Proc. Royal Soc. London A. 225, No. 7 pp. 199-245.

9. Francis, M., "A Wind Tunnel Investigation of the Formation of a Trailing Vortex," Ph.D. Thesis, U. Colorado (1976).

10. Shamroth, S.J., "A Viscous Flow Analysis for The Tip Vortex Generation Process," NASA CR 318 (1979).

11. Chandrashekhara, N., "Analysis of Tip Vortex Cavitation Inception of Hydrofoils and Propellers," Schiffstechnik, Bd. 23, p. 47 (1976).

12. Noordzij, L., "A Note on the Scaling of Tip Vortex Cavitation Inception," International Shipbuilding Progress, Vol. 24, No. 277 (1977).

13. Crump, S.F., "The Effect of Bulbous Blade Tips on the Development of Tip-Vortex Cavitation on Model Marine Propellers (U)," NSRDC Report C-99 (Mar 1948).

14.   White, R.P., Jr. and J.C. Balcerk, "Investigation of the Dissipation of the Tip Vortex of a Rotor Blade by Mass Injection," U.S. Army Air Mobility Research and Development Laboratory Report 72-43, Contract to Rochester Appl. Sci. Assoc., RASA Report 72-03 (Aug 1972).

15.   Spencer, R.N. et al., "Tip Vortex Core Thickening for Application to Helicopter Rotor Noise Reduction," U.S. Army Aviation Materials Laboratory Technical Report 66-1 (Sep 1966).

16.   Wood, K.D., "Aerospace Vehicle Design--Volume 1, Aircraft Design," Boulder Research Associates (1969).

17.   Schlichting, H., "Boundary Layer Theory," McGraw-Hill Book Co. (1960).

18.   Kuiper, G., "Modeling of Tip Vortex Cavitation on Ship Propellers," 4th Lips Propeller Symposium, Drunen, The Netherlands (Oct 1979).

19.   Spreiter, J.R. and A.H. Sacks, "The Rolling Up of the Trailing Vortex Sheet and Its Effect on the Downwash Behind Wings," J. Aeronaut. Sci., pp. 21-33 (Jan 1951).

20.   Brockett, T., "Minimum Pressure Envelopes for Modified NACA 66 Sections with NACA a = 0.8 Camber and Buships Type I and Type II Sections," DTMB Report 1780 (Feb 1966).

21.   Arndt, R.E.A. et al., "Influence of Surface Irregularities on Cavitation Performance," Journal of Ship Research, Vol. 23, No. 3 (Sep 1979).

22. Hoerner, S.F., "Fluid Dynamic Drag," publ. by Author, United States Library of Congress No. 64-19666 (1965).

23.   Granville, P.S., "The Determination Of the Local Skin Friction and the Thickness of Turbulent Boundary Layers From the Velocity Simlarity Laws," DTMB Report 1340 (Oct 1959).

24.   Daily, J.W. and D.R. Harleman, "Fluid Mechanics," Addison-Wesely Book Co. (1966).

Copies			Copies		
1	ARMY CHIEF OF RES & DEV			NAVSEASYSCOM (Continued)	
			3	SEA 521	
1	ARMY ENGR R&D LAB		1	SEA 522	
			2	SEA 524	
2	CNR		1	SEA 525	
	1	Code 438	1	SEA 08	
	1	LIB	2	SEA 99632	
			1	PMS 378	
1	NRL		1	PMS 380	
			1	PMS 381	
4	ONR BOSTON		1	PMS 383	
			1	PMS 389	
4	ONR CHICAGO		1	PMS 391	
			1	PMS 392	
4	ONR LONDON, ENGLAND		1	PMS 393	
			1	PMS 397	
4	ONR PASADENA		1	PMS 399	
3	USNA				
	1 LIB		1	NAVSEC 6600 NORFOLK VA	
	1 JOHNSON				
	1 McCORMICK		1	NAVFACENGCOM 032C	
1	NAVPGSCOL LIB		1	MILITARY SEALIFT COMMAND (M-4EX)	
1	NROTC & NAVADMINU, MIT				
			1	NAVSHIPYD/CHASN	
1	NAVAIRDEVCEN				
			1	NAVSHIPYD/LBEACH	
6	NAVOCEANSYSCEN				
	1	1311/LIB	1	NAVSHIPYD/MARE	
	1	13111/LIB			
	1	REISCHMAN	1	NAVSHIPYD/NORVA	
	1	NELSON			
	1	GREEN	1	NAVSHIPYD/PEARL	
	1	DONOHUE			
			1	NAVSHIPYD/PHILA	
39	NAVSEASYSCOM				
	1	SEA 03D	1	NAVSHIPYD/PTSMH	
	1	SEA 031			
	5	SEA 033	1	NAVSHIPYD/PUGET	
	1	SEA 034			
	1	SEA 312	12	DTIC	
	1	SEA 32			
	1	SEA 321	1	BUSTAND/KLEBANOFF	
	4	SEA 05D			
	2	SEA 05H	2	HQS COGARD	
	1	SEA 52P			
	1	SEA 52	1	US COAST GUARD (G-ENE-4A)	

Copies			Copies	
1	LC/SCI & TECH DIV		1	FLORIDA ATLANTIC U/OE LIB
9	MARAD		3	HARVARD U
	1 DIV SHIP DES			1 MCKAY LIB
	1 COORD RES			1 BIRKOFF
	1 DASHNAW			1 CARRIER
	1 FALLS			
	1 HAMMER		2	U HAWAII/BRETSCHNEIDER
	1 LASKY			
	1 NACHTSHEIM		1	U ILLINIOS/ROBERTSON
	1 SCHUBERT			
	1 SIEBOLD		2	U IOWA
				1 IHR/KENNEDY
2	MMA			1 IHR/LANDWEBER
	1 LIB			
	1 MARITIME RES CEN		2	JOHNS HOPKINS U
				1 PHILLIPS
2	NASA STIF			1 INST COOP RES
	1 DIR RES			
			1	U KANSAS/CIV ENGR LIB
1	NSF ENGR DIV LIB			
			1	KANSAS ST U ENGR EXP/NESMITH
1	DOT LIB			
			1	LEHIGH U FRITZ ENGR LAB/LIB
1	U BRIDGEPORT/URAM			
			1	LONG ISLAND U
2	U CAL BERKELEY			
	1 DEPT NAME		1	U MARYLAND/GLEN MARTIN INST
	1 WEHAUSEN			
			5	MIT
1	U CAL SAN DIEGO/ELLIS			1 OCEAN ENGR/LIB
				1 OCEAN ENGR/KERWIN
2	US SCRIPPS			1 OCEAN ENGR/LEEHEY
	1 POLLACK			1 OCEAN ENGR/LYON
	1 SILVERMAN			1 OCEAN ENGR/NEWMAN
4	CIT		7	U MICHIGAN
	1 AERO LIB			1 NAME LIB
	1 ACOSTA			1 NAME/COUCH
	1 PLESSET			1 DEPT/HAMMITT
	1 WU			1 NAME/OGILVIE
				1 WILLOW RUN LABS
1	CATHOLIC U			1 NAME/VORUS
				1 NAME/LATORRE
2	COLORADO STATE U/ALBERTSON			
	1 TULLIS			
1	U CONNECTICUT/SCOTTRON			
1	CORNELL U/SEARS			

57

Copies

1	EASTERN RES GROUP
1	EXXON DES DIV
1	FRIEDE & GOLDMAN/MICHEL
1	GEN DYN CONVAIR ASW—MARINE SCIENCES
1	GEN DYN ELEC BOAT/BOATWRIGHT

3	GIBBS & COX
	  1 TECH LIB
	  1 CAPT NELSON
	  1 OLSON

1	GRUMMAN AEROSPACE/CARL

2	HYDROMECH RES ASSOC
	  1 COX
	  1 NELKA

2	HYDRONAUTICS
	  1 SCHERER
	  1 LIB

1	INGALLS SHIPBUILDING
1	INST FOR DEFENSE ANAL
1	ITEK VIDYA
1	LITTLETON R & ENGR CORP/REED
1	LITTON INDUSTRIES
1	LOCKHEED M & S/WAID

2	MARINE VIBRATION ASSOC
	  1 BRADSHOW
	  1 VASSILOPOULIS

1	NAR SPACE/UJIHARA
1	NATIONAL STEEL & SHIPBLDG
1	NEWPORT NEWS SHIPBLDG/LIB
1	NIELSON ENGR/SPANGLER

Copies

1	PROPULSION DYNAMICS, INC
1	K.E. SCHOENHERR
1	GEORGE G. SHARP
1	SCIENTIFIC RES ASSC/SHAMROTH
1	SPERRY SYS MGMT LIB/SHAPIRO
1	ROBERT TAGGART
1	TETRA TECH PASADENA/CHAPKIS
1	TRACOR
1	UNITED AIRCRAFT HAMILTON STANDARD/CORNELL

CENTER DISTRIBUTION

Copies	Code	Name
1	11	W. Ellsworth
1	15	W. Morgan
1	1507	D.S. Cieslowski
1	1509	H. Pollard
1	152	W. Lin
1	1524	
1	1524	W. Day
1	1524	K. Remmers
1	1524	R. Roddy
1	1532	G. Dobay
1	154	J. McCarthy
1	1543	R. Cumming
1	1544	R. Boswell
1.	1544	E. Caster
1	1544	D. Fuhs
1	1544	S. Jessup
20	1544	G. Platzer
1	1552	T. Brockett
1	1552	T. Huang
1	1556	P. Besch
1	1556	D. Coder

Copies	Code	Name
1	1556	G. Santore
20	1556	W. Souders
1	156	G. Hagen
1	1576	R. Hecker
1	172	M. Krenzke
1	1720.6	R. Rockwell
1	1802	H. Lugt
1	19	M. Sevik
1	1905	W. Blake
1	192	R. Biancardi
1	194	J. Shen
1	1942	F. Archibald
1	1942	R. Armstrong
1	1942	E. Geib
1	1962	C. Noonan
1	1962	A. Zaloumis
1	2940	J. Stevens
10	5211.1	Reports Distribution
1	522.1	Library (C)
1	522.2	Library (A)

DTNSRDC ISSUES THREE TYPES OF REPORTS

1. DTNSRDC REPORTS, A FORMAL SERIES, CONTAIN INFORMATION OF PERMANENT TECH-
NICAL VALUE. THEY CARRY A CONSECUTIVE NUMERICAL IDENTIFICATION REGARDLESS OF
THEIR CLASSIFICATION OR THE ORIGINATING DEPARTMENT.

2. DEPARTMENTAL REPORTS, A SEMIFORMAL SERIES, CONTAIN INFORMATION OF A PRELIM-
INARY, TEMPORARY, OR PROPRIETARY NATURE OR OF LIMITED INTEREST OR SIGNIFICANCE.
THEY CARRY A DEPARTMENTAL ALPHANUMERICAL IDENTIFICATION.

3. TECHNICAL MEMORANDA, AN INFORMAL SERIES, CONTAIN TECHNICAL DOCUMENTATION
OF LIMITED USE AND INTEREST. THEY ARE PRIMARILY WORKING PAPERS INTENDED FOR IN-
TERNAL USE. THEY CARRY AN IDENTIFYING NUMBER WHICH INDICATES THEIR TYPE AND THE
NUMERICAL CODE OF THE ORIGINATING DEPARTMENT. ANY DISTRIBUTION OUTSIDE DTNSRDC
MUST BE APPROVED BY THE HEAD OF THE ORIGINATING DEPARTMENT ON A CASE-BY-CASE
BASIS.